



AFRL-RB-WP-TR-2008-3019

**ADVANCES IN HIGH-FIDELITY MULTI-PHYSICS
SIMULATION TECHNIQUES**

Datta Gaitonde, Eswar Josyula, and Miguel Visbal

**Computational Sciences Branch
Aeronautical Sciences Division**

**JANUARY 2008
Final Report**

Approved for public release; distribution unlimited.

See additional restrictions described on inside pages

STINFO COPY

**AIR FORCE RESEARCH LABORATORY
AIR VEHICLES DIRECTORATE
WRIGHT-PATTERSON AIR FORCE BASE, OH 45433-7542
AIR FORCE MATERIEL COMMAND
UNITED STATES AIR FORCE**

NOTICE AND SIGNATURE PAGE

Using Government drawings, specifications, or other data included in this document for any purpose other than Government procurement does not in any way obligate the U.S. Government. The fact that the Government formulated or supplied the drawings, specifications, or other data does not license the holder or any other person or corporation; or convey any rights or permission to manufacture, use, or sell any patented invention that may relate to them.

This report was cleared for public release by the Air Force Research Laboratory Wright-Patterson Air Force Base (AFRL/WPAFB) Public Affairs Office and is available to the general public, including foreign nationals. Copies may be obtained from the Defense Technical Information Center (DTIC) (<http://www.dtic.mil>).

AFRL-RB-WP-TR-2008-3019 HAS BEEN REVIEWED AND IS APPROVED FOR PUBLICATION IN ACCORDANCE WITH ASSIGNED DISTRIBUTION STATEMENT.

*//Signature//

DATTA GAITONDE, Technical Area Leader
Computational Sciences Branch
Aeronautical Sciences Division

//Signature//

REID MELVILLE, Chief
Computational Sciences Branch
Aeronautical Sciences Division

//Signature//

MATTHEW BURKINSHAW, Technical Advisor
Computational Sciences Branch
Aeronautical Sciences Division

This report is published in the interest of scientific and technical information exchange, and its publication does not constitute the Government's approval or disapproval of its ideas or findings.

*Disseminated copies will show “//Signature//” stamped or typed above the signature blocks.

REPORT DOCUMENTATION PAGE				<i>Form Approved</i> OMB No. 0704-0188	
<p>The public reporting burden for this collection of information is estimated to average 1 hour per response, including the time for reviewing instructions, searching existing data sources, gathering and maintaining the data needed, and completing and reviewing the collection of information. Send comments regarding this burden estimate or any other aspect of this collection of information, including suggestions for reducing this burden, to Department of Defense, Washington Headquarters Services, Directorate for Information Operations and Reports (0704-0188), 1215 Jefferson Davis Highway, Suite 1204, Arlington, VA 22202-4302. Respondents should be aware that notwithstanding any other provision of law, no person shall be subject to any penalty for failing to comply with a collection of information if it does not display a currently valid OMB control number. PLEASE DO NOT RETURN YOUR FORM TO THE ABOVE ADDRESS.</p>					
1. REPORT DATE (DD-MM-YY) January 2008		2. REPORT TYPE Final		3. DATES COVERED (From - To) 01 December 1997 – 31 December 2007	
4. TITLE AND SUBTITLE ADVANCES IN HIGH-FIDELITY MULTI-PHYSICS SIMULATION TECHNIQUES				5a. CONTRACT NUMBER In-house	
				5b. GRANT NUMBER	
				5c. PROGRAM ELEMENT NUMBER 0601102	
6. AUTHOR(S) Datta Gaitonde, Eswar Josyula, and Miquel Visbal				5d. PROJECT NUMBER A03S	
				5e. TASK NUMBER	
				5f. WORK UNIT NUMBER 0B	
7. PERFORMING ORGANIZATION NAME(S) AND ADDRESS(ES) Computational Sciences Branch, Aeronautical Sciences Division Air Force Research Laboratory, Air Vehicles Directorate Wright-Patterson Air Force Base, OH 45433-7542 Air Force Materiel Command United States Air Force				8. PERFORMING ORGANIZATION REPORT NUMBER AFRL-RB-WP-TR-2008-3019	
9. SPONSORING/MONITORING AGENCY NAME(S) AND ADDRESS(ES) Air Force Research Laboratory Air Vehicles Directorate Wright-Patterson Air Force Base, OH 45433-7542 Air Force Materiel Command United States Air Force				10. SPONSORING/MONITORING AGENCY ACRONYM(S) AFRL/RBAC	
				11. SPONSORING/MONITORING AGENCY REPORT NUMBER(S) AFRL-RB-WP-TR-2008-3019	
12. DISTRIBUTION/AVAILABILITY STATEMENT Approved for public release; distribution unlimited.					
13. SUPPLEMENTARY NOTES PAO Case Number: WPAFB 08-0121, 22 Jan 2008. Report contains color.					
14. ABSTRACT Efforts performed under this task to evolve a high-fidelity methodology for multi-physics applications in all speed regimes are summarized. Among the disciplines considered are fluid dynamics (turbulence, acoustics), electromagnetics, magnetogasdynamics, aero-structural interactions and thermo-chemical nonequilibrium. For high-order accuracy, a compact-difference based method is developed, supplemented by a filtering procedure to guarantee numerical stability in the presence of boundary truncation, stretching and non-linearity. The filter is also shown to be suitable for sub-grid closure within the high-order no-model large-eddy simulation. Further, boundary treatments for domain-decomposition techniques have also been developed. For high-temperature kinetics, accuracy is enforced through development and validation of master-equation and extended Navier-Stokes approaches, which facilitate accounting of detailed energy transfers between vibrational, rotational and translational modes, and their impact on dissociation.					
15. SUBJECT TERMS high-fidelity simulation, multi-physics analysis, thermochemical nonequilibrium					
16. SECURITY CLASSIFICATION OF:			17. LIMITATION OF ABSTRACT: SAR	18. NUMBER OF PAGES 60	19a. NAME OF RESPONSIBLE PERSON (Monitor) Datta Gaitonde 19b. TELEPHONE NUMBER (Include Area Code) N/A
a. REPORT Unclassified	b. ABSTRACT Unclassified	c. THIS PAGE Unclassified			

Table of Contents

Section	Page
List of Figures	v
Acknowledgements	vii
1 Introduction	1
2 High-Order Methodology for Fluid Dynamics and Electromagnetics	3
2.1 Governing Equations	3
2.2 Numerical Technique	5
2.2.1 Difference Scheme	5
2.2.2 Filtering Scheme	6
2.2.3 Time-integration Schemes	7
2.2.4 Spatial and Temporal Metric Evaluation	8
2.2.5 Interface Treatment in Multidomain Calculations	9
2.2.6 Mesh Overlap Configuration	10
2.2.7 Three-point overlap results	11
2.2.8 Effect of Overlap Size	12
2.2.9 Curvilinear Multidomain Calculations	13
2.2.10 Viscous Multidomain Calculations	14
2.3 Applications	16
2.4 Fluid Dynamics	16
2.5 Wave Propagation – Electromagnetics	19
2.6 Magnetogasdynamics	20
3 High-temperature molecular kinetics methodology	22
3.1 Theoretical Model	24
3.2 Multitranslational Temperature Modeling	25
3.3 Rotational Temperature Modeling	28
3.4 Multiquantum Energy Exchanges in the Vibrational Manifold	30
3.5 Vibrational Bias and Depletion in Dissociation	31
3.6 Results and Discussion	34
3.7 Multitranslational and Rotational Temperatures in Shock Structure	34
3.8 Effect of MultiQuantum V-T Exchanges on Vibrational Temperatures in Blunt Body Flows	35
3.9 Effect of Vibrational Bias in Blunt Body Flows	38

Section	Page
4 Conclusions	42
5 References	43
List of Acronyms, Abbreviations and Symbols	47

List of Figures

Figures	Page
1 Single-Domain Calculation on 30×60 Mesh	9
2 Schematic of Mesh Overlap with Five Points	10
3 Multidomain Computation with Three-Point Vertical Overlap	11
4 Effect of Higher Order Formulas With three-Point Vertical Overlap	12
5 Effect of Overlap Size on Swirl Velocity Along Centerline at $T = 12$	13
6 multidomain Computations with Five-Point Horizontal Overlap	14
7 Propagation of Vortex on Multidomain Curvilinear Mesh	15
8 Multidomain Flat-Plate Boundary Layer Computation with Five-Point Overlap	16
9 Shedding Past a Cylinder at $Re = 100$	17
10 Application to Fluid Dynamics: Vorticity Field in Vortex Breakdown over Delta Wing	18
11 Application to Fluid Dynamics: Simulation of a Forced Transitional Wall-Jet	18
12 Application to Electromagnetics: Radar Cross Section of a Sphere at $ak = 4.0$ and $ak = 7.0$	20
13 Application to Magnetogasdynamics: Control of Flow in a Channel with Transverse Magnetic Field	21
14 Schematic Showing Multiquantum Transitions in Vibrational States and Dis- sociation	23
15 Multiquantum V-T Transition Rates for five Quantum Levels at 1000 K for the N_2 Molecule	29
16 Multiquantum V-T Transition Rates for Five Quantum Levels at 10000K for the N_2 Molecule	31
17 Typical Computational Grid for Blunt Body Flow	34
18 Computed Normalized Density and Temperatures for a Mach 1.2 Maxwellian Gas Shock Wave	35
19 Computed Normalized Density and Temperatures for a Mach 2.0 Maxwellian Gas Shock Wave	36
20 Computed Normalized Density and Temperatures for a Mach 5.0 Maxwellian Gas Shock Wave	36
21 Comparison of Temperatures Along Stagnation Streamline and Along Surface for Nitrogen Flow Past Blunt Body	37
22 Population Distribution at Select Locations Along Stagnation Streamline for Nitrogen Flow Past Blunt Body	37

Figures	Page
23 Comparison of Vibrational Biases on the Effective Dissociation Rate Coefficient	38
24 Dissociation Reduction Factor for Oxygen and Nitrogen Due to Depletion . .	39
25 Effect of Vibrational Bias and Depletion in Blunt Body Flow on Temperature and Dissociation Rate)	40
26 Comparison of Translational and Vibrational Temperature Along the Stagna- tion Streamline	41
27 Comparison of Shock-Standoff Distances	41

Acknowledgements

This work was supported by grants from the Air Force Office of Scientific Research and high performance computing time from the Department of Defense High Performance Computing Modernization Program through centers at the Aeronautical Systems Center, Naval Oceanographic Office, Engineer Research and Development Center and the Army High Performance Research Center.

1 Introduction

The development of future aerospace vehicles requires the optimization and coupling of diverse technologies in order to operate under stringent conditions near the performance envelope. The design of such vehicles is critically dependent on simulation tools which integrate several fundamental disciplines and which necessarily exploit the power of advanced parallel computing platforms. The motivation to develop high-fidelity algorithms derives from considerations in various areas of current interest. For example, in fluid dynamics, the effort to minimize the impact of aerodynamically generated sound on communities and structures has necessitated large-scale time-domain aeroacoustics computations.¹ Another field where numerically intensive wave-propagation phenomena dominate is in electromagnetic wave scattering, which is crucial in determination of radar signature and in biomedical modeling. Similarly, in the field of turbulence simulation, methods to overcome the traditional limitations of Reynolds-averaged approaches have focused on direct- and large-eddy simulation techniques which seek to resolve the multispectral, highly nonlinear stochastic phenomena from computationally challenging first principles. Endeavors which combine fluid dynamics with other disciplines also yield a large and typically stiff equation set whose numerical solution mandates the development and utilization of high-resolution techniques. One example is the complex flow-acoustic-structural interaction which gives rise to practically significant phenomena including panel flutter, transition delay, drag and noise reduction, turbulent flow sensing and modification, and control of unsteady separation by means of deforming flexible surfaces. Another area of great current focus, magnetogasdynamic flow control, derives from the integration of fluid dynamics with electromagnetics and models of thermochemical nonequilibrium. The potential benefits include drastic reductions of thermomechanical fluid load and control of transition, turbulence and separation, without the deployment of moving surfaces, which is a very attractive option at hypersonic speeds.

The equations governing the behavior of the above phenomena of interest exhibit a wide range of mathematical properties and are described in Section 2.1. The high-resolution method required to resolve the stiff spatiotemporal scales must also, therefore, exhibit highly flexible traits necessary for uniform applicability, with little regard to the structure of the equation set. Additional difficulties arise from the fact that modern computational methods require focus on practical problems with their attendant geometrical complexity. Configurations of interest are typically three-dimensional and numerical simulation is greatly facilitated by curvilinear or body-fitted coordinate systems. Since the phenomena are typically unsteady, and boundaries may be flexible, the ability to treat deforming meshes is also essential.

A survey of the literature indicates a clear requirement for new versatile high-resolution methodologies to address the sophisticated design space described above. In this report, a powerful combination of very high-order finite-difference schemes is developed, which fulfils this need. The method is based on compact (Padé-type) formulas^{2,3} of fourth- and sixth-order accuracy, which are employed to form the various derivatives (Section 2.2.1). Although these schemes have a long history, their use has been restricted to geometrically simple situations in which uniform meshes suffice and boundaries may be treated

simplistically. Application to practical multidisciplinary problems has languished due to their extreme susceptibility to numerical instabilities which are initiated at mesh nonuniformities and at truncated boundaries and which subsequently grow unbounded. To overcome these difficulties, the present effort supplements the difference schemes with filters.^{3,4} This component is also Padé-type as described in Section 2.2.2 and is utilized in a post-processing framework to remove high-frequency oscillations which are not supportable on the meshes employed.

Several adequate time-marching methods are available for use with spatially high-order accurate methods. As described in Section 2.2.3, here we adopt the classical fourth-order four-stage Runge-Kutta method for primary use in wave propagation dominated situations. On fine and stretched meshes of the type employed in wall-bounded flows, this explicit scheme is unacceptably restricted in allowable time-step-size. In such cases, an implicit, up to third-order accurate approximately factored scheme is employed within a sub-iteration framework.

The difficulties associated with the use of higher order schemes on general curvilinear meshes are not restricted to the appearance of numerical instabilities. A potentially debilitating source of error is associated with the failure to preserve freestream when metrics are evaluated in the standard manner. In Section 2.2.4, elegant procedures are developed to eliminate this source of inaccuracy without significant computational penalty.

The rapid gain in popularity of relatively cheap parallel computing platforms effectively demands that new computational techniques be capable of exploiting distributed processing strategies. Padé-type methods are not trivially adaptable to such approaches due to their implicit nature. In Section 2.2.5, a domain-decomposition technique is derived for arbitrary meshes. The key element is a multipoint overlap procedure to treat the artificial boundaries created at domain interfaces in general curvilinear grids.

To validate the method and to highlight its properties, Section 2.3 discusses several applications in some of the areas of interest noted above. For the purposes of brevity, these represent only a small subset of the problems examined but nonetheless emphasize the versatility of the approach.

In addition to broad spatio-temporal scales, high-fidelity methods are also required for multifluid problems associated with thermochemical nonequilibrium. For this class of problems, an effort is described to understand the interaction between various molecular kinetic modes such as vibration-vibration (V-V) and vibration-translation (V-T), which have a profound impact on the performance of high-speed devices. Vibrational freezing in the nozzle of a high-speed propulsion engine represents wasted energy that is not recovered as thrust work. A prerequisite to minimizing this loss is to develop an understanding of the dominant thermochemical processes. In Section 3, advances in Master and extended Navier-Stokes simulation techniques, defining the physics of the vibrational manifold are documented.

2 High-Order Methodology for Fluid Dynamics and Electromagnetics

2.1 Governing Equations

In order to highlight the multidisciplinary nature of the compact-difference-based technique, consider a generic governing equation system written in curvilinear coordinates ($\xi = \xi(x, y, z, t)$, $\eta = \eta(x, y, z, t)$, $\zeta = \zeta(x, y, z, t)$, $\tau = t$) in nondimensional, strong-conservation form:

$$\frac{\partial}{\partial \tau} \left(\frac{Q}{J} \right) + \frac{\partial \hat{F}}{\partial \xi} + \frac{\partial \hat{G}}{\partial \eta} + \frac{\partial \hat{H}}{\partial \zeta} = \frac{S}{J}. \quad (1)$$

Here Q denotes the solution vector, $J = \partial(\xi, \eta, \zeta, \tau) / \partial(x, y, z, t)$ is the transformation Jacobian and S is a source vector. The form of the flux vectors \hat{F} , \hat{G} and \hat{H} depends on the nature of the problem being solved and may, in general be written in terms of the corresponding Cartesian flux vectors, F , G and H . For example,

$$\hat{F} = \frac{1}{J}(\xi_x F + \xi_y G + \xi_z H). \quad (2)$$

Various physical models may be obtained by suitably choosing the vectors in Equation 1. For brevity, in the following we focus primarily on the vectors Q , F and \hat{F} with the understanding that other vectors may be written in an analogous fashion or obtained from the citations provided. The Euler equations are obtained (see e.g., Ref. 5 for details) when Q is the five-component vector, $\{\rho, \rho u, \rho v, \rho w, \rho E\}$, $S = 0$ and $F = F_I$ where

$$F_I = \begin{bmatrix} \rho u \\ \rho u^2 + p \\ \rho uv \\ \rho uw \\ (\rho E + p) u \end{bmatrix}. \quad (3)$$

For subsequent reference, $\hat{F} = \hat{F}_I$ for the Euler equations in curvilinear coordinates is given by

$$\hat{F}_I = \begin{bmatrix} \rho \hat{U} \\ \rho u \hat{U} + \hat{\xi}_x p \\ \rho v \hat{U} + \hat{\xi}_y p \\ \rho w \hat{U} + \hat{\xi}_z p \\ (\rho E + p) \hat{U} - \hat{\xi}_t p \end{bmatrix}. \quad (4)$$

In these equations, ρ is the density, u, v, w are Cartesian components of the velocity, p is the static pressure, E is the total energy, $p/(\gamma - 1)\rho + (u^2 + v^2 + w^2)/2$, \hat{U} is the contravariant velocity vector, $\hat{U} = \hat{\xi}_t + \hat{\xi}_x u + \hat{\xi}_y v + \hat{\xi}_z w$, and $\hat{\xi}_t = J^{-1}\xi_t$, $\hat{\xi}_x = J^{-1}\xi_x$, ... denote the metrics of the coordinate transformation.

The Navier-Stokes equations may be obtained by adding components associated with the viscous fluxes, i.e., $F = F_I + F_V$ where

$$F_V = \left\{ \begin{array}{c} 0 \\ \frac{1}{Re} \tau_{xx} \\ \frac{1}{Re} \tau_{xy} \\ \frac{1}{Re} \tau_{xz} \\ \frac{1}{Re} (u\tau_{xx} + v\tau_{xy} + w\tau_{xz}) + \frac{\mu}{(\gamma-1)PrM^2Re} \frac{\partial T}{\partial x} \end{array} \right\}. \quad (5)$$

Here, $\tau_{xx}, \tau_{xy}, \dots$ denote components of the stress tensor (see Ref. 5 for detailed formulas), Re is the Reynolds number, M and Pr are the Mach and Prandtl numbers, T is the temperature and γ is the ratio of specific heats.

To express Maxwell's equations in the template of Equation 1, Q may be set to, $Q = \{E_x, E_y, E_z, B_x, B_y, B_z\}$ and

$$F = \left\{ \begin{array}{c} 0 \\ \frac{B_z}{\mu_m \epsilon} \\ -\frac{B_y}{\mu_m \epsilon} \\ 0 \\ -\frac{E_z}{\mu_m} \\ \frac{E_y}{\mu_m} \end{array} \right\}. \quad (6)$$

where μ_m and ϵ are the permeability and permittivity of free space and $\vec{E} = \{E_x, E_y, E_z\}$ and $\vec{B} = \{B_x, B_y, B_z\}$ are the electric field and magnetic induction vectors respectively.

The governing equations of magnetogasdynamics are obtained by combining Maxwell's and Navier-Stokes equations, together with Ohm's law, under the assumption that relativistic effects may be ignored and that the displacement current is small.⁶ In this case, Q in Equation 1 is set to the eight-component vector $\{\rho, \rho u, \rho v, \rho w, \rho E, B_x, B_y, B_z\}$ where the total energy E now includes components associated with the magnetic field, $E = p/((\gamma - 1)\rho) + (u^2 + v^2 + w^2)/2 + R_b \vec{B} \cdot \vec{B}/(2\mu_m \rho)$. Correspondingly,

$$F = \left\{ \begin{array}{c} \rho u \\ \rho u^2 + P - R_b \frac{B_x}{\mu_m} B_x \\ \rho uv - R_b \frac{B_y}{\mu_m} B_x \\ \rho uw - R_b \frac{B_z}{\mu_m} B_x \\ (\rho E + P)u - R_b \left(\vec{U} \cdot \frac{\vec{B}}{\mu_m} \right) B_x \\ 0 \\ uB_y - vB_x \\ uB_z - wB_x \end{array} \right\}. \quad (7)$$

where $P = p + \frac{B^2}{2\mu_m}$ is the sum of the static (p) and magnetic pressures, and

$$F_V = \left\{ \begin{array}{c} 0 \\ \frac{1}{Re} \tau_{xx} \\ \frac{1}{Re} \tau_{xy} \\ \frac{1}{Re} \tau_{xz} \\ \hline \frac{1}{Re} (u\tau_{xx} + v\tau_{xy} + w\tau_{xz}) + \frac{1}{(\gamma-1)PrM^2 Re} \frac{\partial T}{\partial x} + \\ \frac{R_b}{R_\sigma} \left\{ \frac{B_y}{\mu_m \sigma} \left(\frac{\partial B_y}{\partial x \mu_m} - \frac{\partial B_x}{\partial y \mu_m} \right) + \right. \\ \left. \frac{B_z}{\mu_m \sigma} \left(\frac{\partial B_z}{\partial x \mu_m} - \frac{\partial B_x}{\partial z \mu_m} \right) \right\} \\ \hline 0 \\ \frac{1}{Re_\sigma} \frac{1}{\sigma} \left(\frac{\partial B_y}{\partial x \mu_m} - \frac{\partial B_x}{\partial y \mu_m} \right) \\ \frac{1}{Re_\sigma} \frac{1}{\sigma} \left(\frac{\partial B_z}{\partial x \mu_m} - \frac{\partial B_x}{\partial z \mu_m} \right) \end{array} \right\}. \quad (8)$$

Here σ is the electrical conductivity, $R_b = \frac{B_{ref}^2}{\rho_{ref} U_{ref}^2 \mu_{mref}}$ is the magnetic pressure number and $R_\sigma = LU_{ref} \mu_{mref} \sigma_{ref}$ is the magnetic Reynolds number.

It is important to recognize that in writing the governing equations in strong conservation form, Equation 1, the following metric identities have been invoked:

$$I_1 = (\hat{\xi}_x)_\xi + (\hat{\eta}_x)_\eta + (\hat{\zeta}_x)_\zeta = 0. \quad (9)$$

$$I_2 = (\hat{\xi}_y)_\xi + (\hat{\eta}_y)_\eta + (\hat{\zeta}_y)_\zeta = 0. \quad (10)$$

$$I_3 = (\hat{\xi}_z)_\xi + (\hat{\eta}_z)_\eta + (\hat{\zeta}_z)_\zeta = 0. \quad (11)$$

$$I_4 = (1/J)_\tau + (\hat{\xi}_t)_\xi + (\hat{\eta}_t)_\eta + (\hat{\zeta}_t)_\zeta = 0. \quad (12)$$

The importance of satisfying these identities in the present higher order finite-difference numerical scheme is detailed in Section 2.2.4.

2.2 Numerical Technique

As noted earlier, a finite-difference approach is adopted to solve the discrete equivalent of the governing equations. Thus, the values of the solution vector are localized in a pointwise sense at each node of the mesh. This considerably simplifies the procedure of formal extension to higher order accuracy and contrasts with the finite-volume approach where cell averaged quantities are typically employed.

2.2.1 Difference Scheme

The approach is illustrated by considering a generic scalar pointwise discrete quantity ϕ . At different stages of the solution procedure, this could be a metric, a primitive variable or a component of a flux vector. In all cases, the required spatial derivative ϕ' is obtained in any transformed coordinate direction by solving the tridiagonal system:

$$\Gamma \phi'_{i-1} + \phi'_i + \Gamma \phi'_{i+1} = b \frac{\phi_{i+2} - \phi_{i-2}}{4} + a \frac{\phi_{i+1} - \phi_{i-1}}{2}. \quad (13)$$

where Γ , a and b determine the spatial properties of the algorithm. Variations of this formula have been described in several references (see for example Ref. 3). It encompasses a family of schemes ranging in accuracy from the standard three-point, second order explicit method (E2), with $\Gamma = 0$, $a = 1$, $b = 0$ to the compact five point, sixth order algorithm (C6) with $\Gamma = \frac{1}{3}$, $a = \frac{14}{9}$, $b = \frac{1}{9}$. Another scheme of interest is the three-point, fourth order method C4 with $\Gamma = \frac{1}{4}$, $a = \frac{3}{2}$, $b = 0$.

The scheme of Equation 13 cannot be applied at a few points near each boundary where the stencil protrudes the domain. Here, special one sided boundary schemes, such as those described in Refs. 7 and 8 are employed. A compendium is provided in Ref. 9.

To compute the residual, the derivatives of the inviscid fluxes are obtained by first forming the fluxes at the nodes and subsequently differentiating each component with the above formulas. Both viscous and nonideal magnetogasdynamic terms, if present, are obtained by first computing derivatives of the primitive variables. The components of the viscous flux are then constructed at each node and differentiated by a second application of the same scheme. Although this approach is not as accurate as that in which a Padé-type scheme is employed directly for the second-derivative, it is significantly cheaper to implement in curvilinear coordinates. A previous effort¹⁰ demonstrates that successive differentiation yields a stable method in conjunction with the added filtering component which is described next.

2.2.2 Filtering Scheme

Compact-difference schemes are susceptible to numerical instability due to their centered, nondiffusive nature. Most problems of practical interest exhibit nonlinear behavior, require domain truncation and nonperiodic boundary conditions. Additionally, the regions of interest are usually discretized with nonuniform meshes. Each of these complications can introduce spurious oscillations which are not damped by centered schemes. Thus, in practical situations, an additional component is required in the method to enforce numerical stability. The approach taken here is to eliminate spurious frequencies through a low-pass filtering procedure.

Denoting a typical component of the solution vector by ϕ , filtered values $\hat{\phi}$ satisfy,

$$\alpha_f \hat{\phi}_{i-1} + \hat{\phi}_i + \alpha_f \hat{\phi}_{i+1} = \sum_{n=0}^N \frac{a_n}{2} (\phi_{i+n} + \phi_{i-n}). \quad (14)$$

This template has been obtained from Refs. 3 and 4. Equation 14 has $N + 2$ unknowns, $\alpha_f, a_0, a_1, \dots, a_N$, which can be derived from Fourier and Taylor-series analyses. The constraints employed include the consideration that the highest (or odd-even) mode be completely annihilated while maintaining higher order accuracy. The coefficients a_0, a_1, \dots, a_N are expressed in terms of α_f which is considered to be a free parameter but must lie in the interval $-0.5 < \alpha_f < 0.5$. Within this range, α_f controls the strength of the filter and as it is reduced, a wider band of frequencies at the higher end of the spectrum is preferentially damped. Computations on a range of 2-D and 3-D problems suggest that on meshes of reasonable quality, a value $0.3 \leq \alpha_f < 0.5$ is appropriate. Only in cases where the mesh is of extremely poor quality, if it contains metric discontinuities for example, a

lower value of $\alpha_f \sim 0.1$ may be required. The impact of filtering on the fully discretized 1-D advection equation with periodic end conditions has been examined in Ref. 11.

The relatively large stencil of very high order filters requires special formulations at several points near the boundaries. For instance, the tenth order interior filter requires an eleven point stencil and thus cannot be applied at the near-boundary points $1, \dots, 5$ and correspondingly at $IL - 4, \dots, IL$ where it protrudes the boundary. The dependent variables at points 1 and IL are specified explicitly through the boundary conditions and are not filtered. At the remaining near-boundary points, two approaches have been developed. In the first, the order of accuracy is reduced on approaching the boundary to the extent necessary for a lower order centered formula to be applicable. Since meshes are usually finer near the boundary, no significant accuracy degradation is observed particularly if a corresponding adjustment (or optimization) of the value of α_f is applied.¹⁰ In the second method, introduced in Ref. 12 higher order one sided formulas have been developed. Although the spectral characteristics of these approaches are nonideal, several applications have demonstrated the elegance of these techniques.¹³

After each time-step, the filter is applied sequentially to the updated solution vector, Q , in each of the three spatial directions. Many other strategies may be suggested but have not yet been explored in the present effort.

2.2.3 Time-integration Schemes

The spatial differencing scheme has been coupled with both explicit and implicit time-integration schemes. The classical fourth order four-stage Runge-Kutta method (RK4), implemented in low-storage form, is utilized primarily for wave propagation problems. Details may be found in Ref. 14 and are not repeated here.

Explicit methods are not suitable however when very fine and highly-stretched meshes are employed as in wall bounded flows. To address this deficiency, a robust and highly accurate implicit procedure has been implemented through the formula:

$$\begin{aligned}
& \left[J^{-1^{p+1}} + \phi^i \Delta \tau \delta_\xi^{(2)} \left(\frac{\partial \hat{F}^p}{\partial Q} \right) \right] J^{p+1} \times \\
& \left[J^{-1^{p+1}} + \phi^i \Delta \tau \delta_\eta^{(2)} \left(\frac{\partial \hat{G}^p}{\partial Q} \right) \right] J^{p+1} \times \\
& \left[J^{-1^{p+1}} + \phi^i \Delta \tau \delta_\zeta^{(2)} \left(\frac{\partial \hat{H}^p}{\partial Q} \right) \right] \Delta Q \\
& = -\phi^i \Delta \tau \left[J^{-1^{p+1}} \frac{(1+\phi)Q^p - (1+2\phi)Q^n + \phi Q^{n-1}}{\Delta \tau} \right. \\
& \quad \left. + Q^p (1/J)_\tau^p + \delta_\xi \left(\hat{F}^p \right) + \right. \\
& \quad \left. \delta_\eta \left(\hat{G}^p \right) + \delta_\zeta \left(\hat{H}^p \right) \right].
\end{aligned} \tag{15}$$

where $\partial \hat{F} / \partial Q$ etc. are flux Jacobians, δ represents the spatial difference operator and $\Delta Q = Q^{p+1} - Q^p$. The method combines the approximate factorization procedure of Ref. 15 with the diagonalized simplification of Ref. 16 and, to reduce errors associated with these simplifications, a sub-iteration strategy is employed. Thus, for the first subiteration, $p = 1$, $Q^p = Q^n$ and as $p \rightarrow \infty$, $Q^p \rightarrow Q^{n+1}$. Typically, three subiterations are applied per time step. Note that while the derivatives of the flux Jacobians have been obtained to second-order accuracy (denoted with the superscript (2)), those on the right hand side, i.e.,

in the residual, are evaluated with the compact-difference based higher order method. In the case of the magnetogasdynamic equations, a loosely coupled approach which separates the flow and magnetic field vectors has been described in Ref. 17. Nonlinear artificial dissipation terms,¹⁸ not explicitly shown in Equation 15, are appended to the implicit operator to enhance stability. Although higher order accuracy in time is achievable with relative ease at the expense of increased storage requirements, a range of numerical experiments suggests that second-order accuracy in time is adequate for the problems considered.¹⁹

2.2.4 Spatial and Temporal Metric Evaluation

As noted earlier, several metric identities (Equations 9 through 12) have been invoked to obtain the strong conservation form of the governing equations, Equation 1. In a finite-difference formulation, spatial and temporal metrics must be evaluated carefully in a manner designed to satisfy these identities numerically so that freestream preservation errors are controlled to within the machine accuracy range.

For the standard second-order explicit method (E2), the straightforward averaging procedure described in Ref. 20 is adequate. However, this technique is not appropriate for higher order methods – it has been shown in Ref. 21 that freestream preservation errors accumulate to the point where the advantages of the new methodology are lost. A similar loss of accuracy occurs when analytic metrics are employed (if available).

To address this important issue, we utilize the formulation developed in the context of lower order methods²² in which the metric relation, for example,

$$\hat{\xi}_x = y_\eta z_\zeta - y_\zeta z_\eta \quad (16)$$

is evaluated by considering the equivalent “conservative” form:

$$\hat{\xi}_x = (y_\eta z)_\zeta - (y_\zeta z)_\eta \quad (17)$$

As demonstrated in Ref.21, this straightforward modification assures that the identities I_1 through I_3 (Equation 9 through Equation 11) are satisfied.

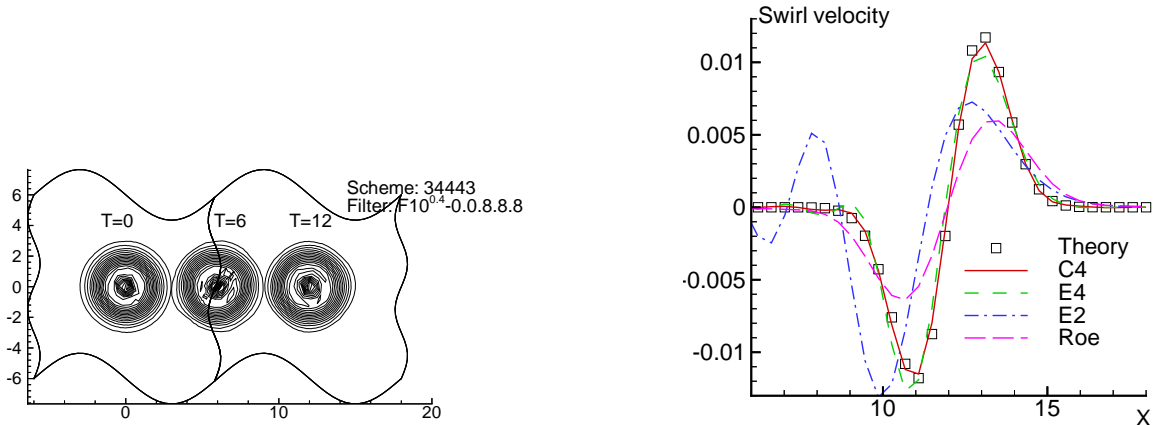
To satisfy the identity I_4 , Equation 12, also known as the Geometric Conservation Law, to numerical accuracy, the remarkably simple approach¹⁹ utilizes I_4 to establish the value for $(1/J)_\tau$, i.e.,

$$(1/J)_\tau = -[(\hat{\xi}_t)_\xi + (\hat{\eta}_t)_\eta + (\hat{\zeta}_t)_\zeta]. \quad (18)$$

where

$$\begin{aligned} \hat{\xi}_t &= -[x_\tau(\hat{\xi}_x) + y_\tau(\hat{\xi}_y) + z_\tau(\hat{\xi}_z)] \\ \hat{\eta}_t &= -[x_\tau(\hat{\eta}_x) + y_\tau(\hat{\eta}_y) + z_\tau(\hat{\eta}_z)] \\ \hat{\zeta}_t &= -[x_\tau(\hat{\zeta}_x) + y_\tau(\hat{\zeta}_y) + z_\tau(\hat{\zeta}_z)]. \end{aligned} \quad (19)$$

This strategy compensates for errors in evaluating time metrics and grid speeds which can then be obtained either by analytic means, if known, or high order discrete approximations.¹⁹



(a) Vorticity contours at three instants with C4- $F10^{0.4}$ scheme

(b) Swirl velocity at $T = 12$ along $Y = 0$ with several schemes

Figure 1: Single-Domain Calculation on 30×60 Mesh

2.2.5 Interface Treatment in Multidomain Calculations

As noted earlier, the major issue in multidomain computations is the treatment of interfaces between domains. In the present work, communication between adjacent meshes is conducted through finite-size overlaps. To explore the issues involved, consider the unsteady inviscid flow due to a convecting vortex in an otherwise uniform flow at a freestream Mach number $M_\infty = 0.1$. The initial condition is determined from the theoretical solution given in Ref. 23. The nondimensional vortex strength parameter, $C/(U_\infty R)$ is set to 0.02 where R is the nominal vortex radius. The domain considered extends $-6 < X = x/R < 18$, $-6 < Y = y/R < 6$. The baseline mesh consists of 60×30 uniformly spaced points, with a spacing $\Delta X = \Delta Y = 0.41$, which is deliberately coarse enough to distinguish between the accuracy of the various schemes. For this problem, the RK4 scheme is employed exclusively, with $\Delta t = 0.005$ which is sufficiently small to guarantee time-step-size independent results on each of the meshes considered.

As a reference, the C4 compact scheme coupled with an interior filter of tenth order accuracy, $F10^{0.4}$ is chosen for analysis. Vorticity contours obtained in a single-domain calculation with periodic end conditions are shown in Figure 1(a) at three instants, $T = 0, 6$ and 12 . At time $t = 0$, the vortex center is located at $X = 0$ and, with increasing time, it convects to the right at a nondimensional velocity of unity. The superiority of C4 over the explicit E4 scheme is clearly demonstrated in Figure 1(b) which shows the swirl velocity along $Y = 0$ at $T = 12$. Results with two lower order schemes are also plotted. The centered E2 scheme shows primarily dispersive error, whereas the popular third-order upwind-biased Roe scheme^{24,25} is highly diffusive.

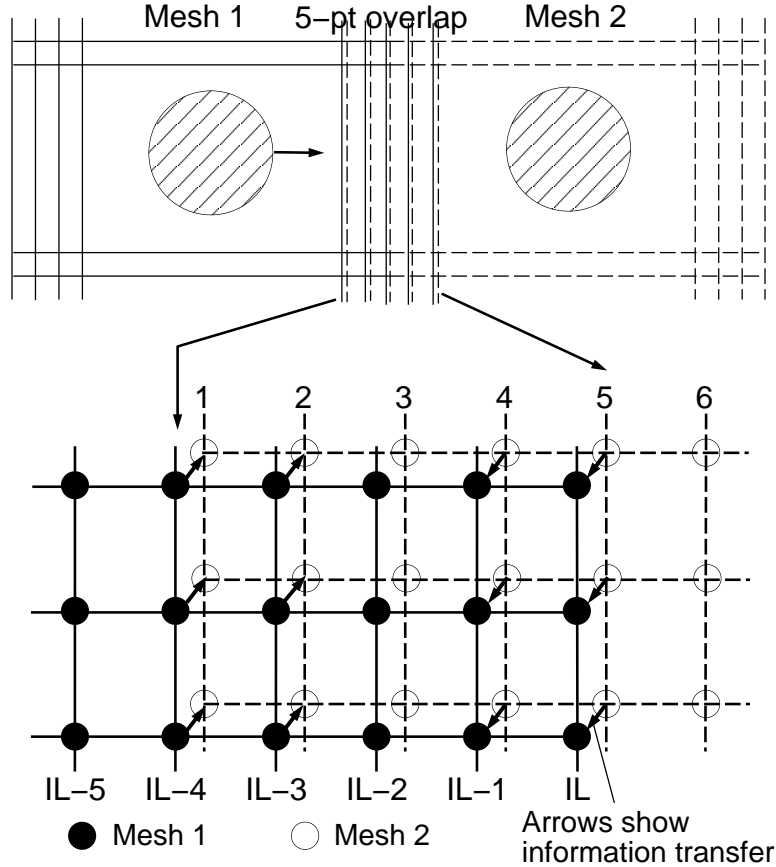
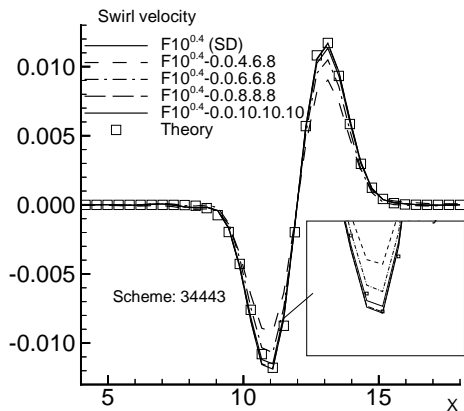


Figure 2: Schematic of Mesh Overlap with Five Points

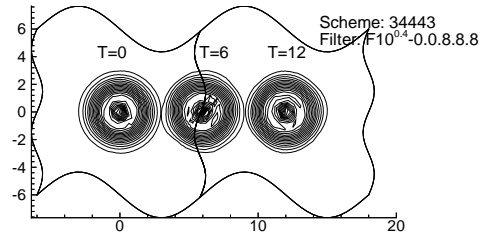
2.2.6 Mesh Overlap Configuration

In the first set of multidomain calculations, a vertical interface is introduced into the above mesh as shown schematically in Figure 2. The computation is started with the vortex located at the center of Mesh 1 (solid lines). With increasing time, the vortex convects into Mesh 2 (dashed lines) after passing through the interface. The meshes communicate through an overlap region. Although the overlap points are collocated, they have been shown slightly staggered in Figure 2 for clarity.

At every time-step, the solution is advanced independently in each domain with individual interior and boundary formulas in the same manner as in single-domain computations. Data is exchanged between adjacent domains at the end of each sub-iteration of the implicit scheme (or each stage of RK4), as well as after each application of the filter. To illustrate data transfer between the domains, details of a five-point vertical overlap is also shown in Figure 2. Each vertical line is denoted by its i -index. The values at points one and two of Mesh 2 are set to be identically equal to the corresponding updated values at points $IL - 4$ and $IL - 3$ of Mesh 1. Similarly, reciprocal information is transferred through points four and five of Mesh 2 which “donate” values to points $IL - 1$ and IL of Mesh 1. This exchange of information is shown with arrows at each point in the schematic. Note that although points on line $IL - 2$ (Mesh 1) and three (Mesh 2) are also collocated,



(a) Swirl velocity at $T = 12$ along horizontal centerline with several schemes coupled with LOC approach



(b) Vorticity contours at three instants with compact difference scheme

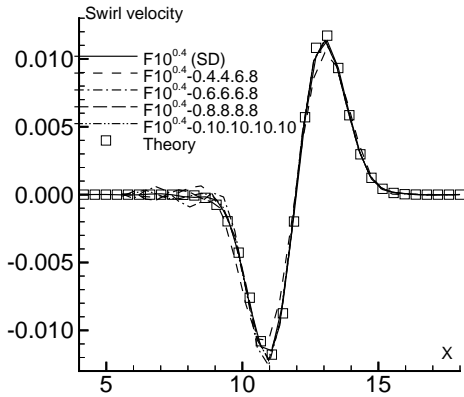
Figure 3: Multidomain Computation with Three-Point Vertical Overlap

they do not communicate directly. This type of point only occurs when the number of overlap points is odd and will be designated the noncommunicating overlap (NCO) point: it facilitates the detection of “drift” between the two solutions.

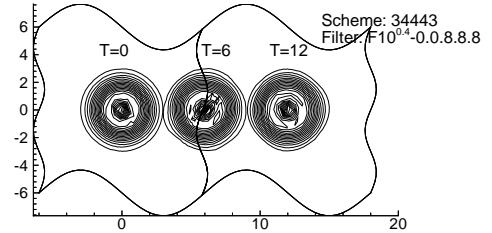
Larger and smaller overlap regions can also be addressed in a similar manner with a minimum of at least two points. At this time overlaps with only an odd number of points have been investigated, specifically those consisting of three, five and seven points. The conclusions derived below are anticipated to carry over to cases with even number of overlap points.

2.2.7 Three-point overlap results

Figure 3(a) exhibits the swirl velocity along the centerline for a three-point overlap i.e., one where each domain obtains information from the other along a single line. Not including the overlap, each mesh now consists of 30×30 points with the NCO occurring at $X = 6$. multidomain calculations with 34443 and 66666 difference schemes are plotted with theory and the single-domain calculation, which is the best achievable result for this purpose. The differencing schemes in the multidomain calculations differ substantially in formal order of accuracy, the first 34443 is formally fourth order accurate by the results of Ref. 26 while the second, 66666, is formally sixth order accurate. Thus, the large swirl velocity errors in the multidomain calculations are not caused by the difference scheme. Subsequent investigations therefore consider only the 34443 scheme. Vorticity contours at three time-instants, shown in Figure 3(b) manifest a large degree of smearing and reduction in peak vorticity values as the disturbance crosses the overlap. Note particularly the contours at $T = 6$ where the vortex appears to elongate as it passes through the interface. The most likely cause of error is the lower order LOC filter formulation employed in each domain near the interface.



(a) Swirl velocity at $T = 12$ along horizontal centerline



(b) Vorticity contours at three instants with compact difference scheme

Figure 4: Effect of Higher Order Formulas With three-Point Vertical Overlap

To test this hypothesis, the LOC approach is replaced with higher order one sided filter formulas developed as part of this effort and presented in Ref. 9. The results show significant improvement in accuracy. Figure 4(a) displays the computed swirl velocity along the centerline with a variety of higher order interface treatments together with the baseline single-domain calculation. The plot indicates that raising the minimum order of accuracy to fourth improves performance substantially with peak error in swirl velocity of only 6 percent compared with 40 percent for the second order LOC method (Figure 3(a)). With a minimum sixth order filter, $F10^{0.4} - 0.6 \cdot 6 \cdot 6 \cdot 8$, the accuracy is comparable to the original single-domain calculation. Further increase in minimum filter order of accuracy to eighth and tenth order has no impact on the solution, which remains stable. Vorticity contours with the $F10^{0.4} - 0.8 \cdot 8 \cdot 8 \cdot 8$ scheme are shown in Figure 4(b) and compare very well with those obtained with the single-domain calculation shown in Figure 1(a).

2.2.8 Effect of Overlap Size

In a three-point overlap, each domain receives data at an end point, which as previously stated is not filtered. By contrast, with larger overlaps (Figure 2), each mesh receives data at several near-boundary points which are set to values obtained from adjacent domains. The filter treatment of these near-boundary points propagates into the interior due to the implicit nature of the Pade-type formulas. In fact, as discussed later, the LOC approach can actually introduce instabilities at domain interfaces. Based on heuristic studies, points receiving data from adjacent domains should preferably be left unfiltered. However, higher order one sided formulas may also be employed. In either case, the minimum order of accuracy increases with overlap size, and consequently interface treatment becomes less critical. This is demonstrated again by plotting swirl velocity along the vortex centerline in Figure 5 for the three, five and seven point overlaps. The seven point overlap computation, which has a minimum sixth order filter, essentially recovers the single domain calculation.

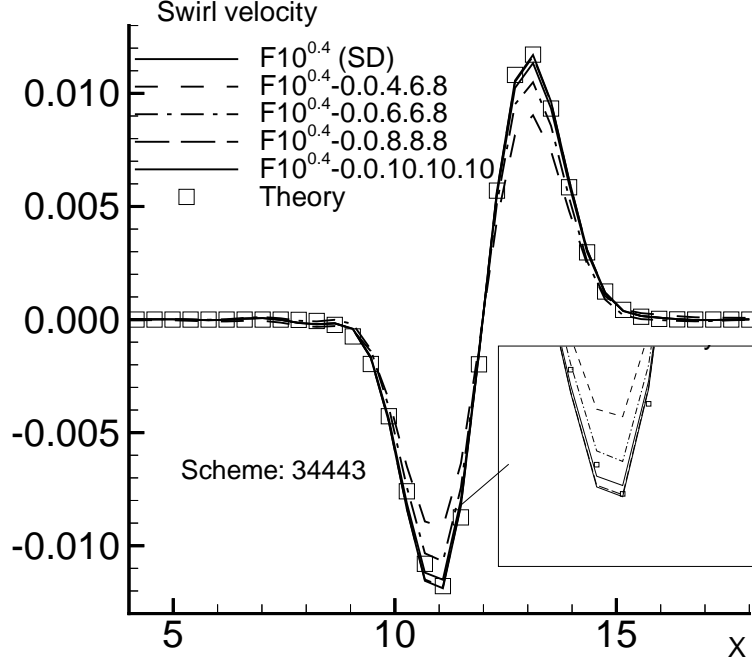


Figure 5: Effect of Overlap Size on Swirl Velocity Along Centerline at $T = 12$

A more challenging problem consists of the case where the original single-domain mesh is split horizontally so that the top part of the vortex is always in Mesh 1 while the lower part is always in Mesh 2 (Figure 6(a)). The performance of several schemes with a five point horizontal overlap is shown in Figure 6(b). The minimum fourth order (LOC) formulation shows considerably higher loss of accuracy compared to the five point vertical overlap calculation of Figure 5. Increasing the minimum order of accuracy brings the results successively closer to the single-domain result. There is little difference between the minimum eighth and tenth order formulations. Vorticity contours obtained with the higher order scheme exhibit negligible distortion as shown in Figure 6(a). In contrast, results with the LOC approach (not shown) indicate that the vortex is diffused and distorted in the direction normal to the interface.

2.2.9 Curvilinear Multidomain Calculations

To demonstrate the use of the interface treatment for a general curvilinear mesh, consider the wavy grid shown in Figure 7(a). The mesh is generated with an extension of the formula described in Ref. 23:

$$\begin{aligned} x_{i,j} &= x_{min} + \Delta x_o \left[(i-1) + A_x \sin\left(\frac{n_x \pi (j-1) \Delta y_o}{L_y} + \frac{i \phi_x}{IL-1}\right) \right] \\ y_{i,j} &= y_{min} + \Delta y_o \left[(j-1) + A_y \sin\left(\frac{n_y \pi (i-1) \Delta x_o}{L_x} + \frac{j \phi_y}{JL-1}\right) \right] \end{aligned} \quad (20)$$

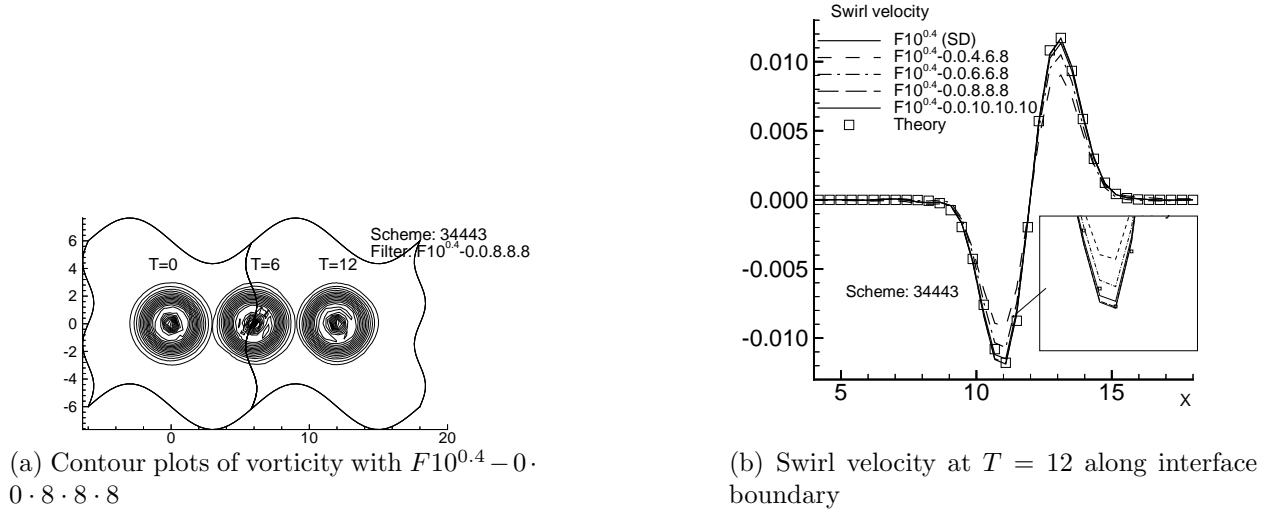


Figure 6: multidomain Computations with Five-Point Horizontal Overlap

$$\Delta x_o = \frac{L_x}{IL-1}, \Delta y_o = \frac{L_y}{JL-1} \quad (21)$$

$$1 \leq i \leq IL, 1 \leq j \leq JL.$$

where IL , JL denote the number of points in the x and y directions and $L_x = x_{max} - x_{min}$ and $L_y = y_{max} - y_{min}$ are the corresponding nominal ranges. The mesh of Figure 7(a) was generated with the parameters $IL = 60$, $JL = 30$, $x_{min} = y_{min} = -6$, $x_{max} = 18$, $y_{max} = 6$, $A_x = 1$, $A_y = 4$, $n_x = 4 = n_y = 4$, $\phi_x = \phi_y = 0$. The resulting mesh has a maximum deviation from orthogonality of 63.1 degrees and a ratio of minimum to maximum Jacobian of 2.1. As before, the 34443 scheme, is retained with a five point overlap. v components of the velocity along the line $j = JL/2$ at $T = 12$ computed with several interface filter formulations are shown in Figure 7(b) together with the single-domain calculation. Each scheme shows some loss of accuracy compared with the equivalent uniform mesh result (see Figure 1(b)). This is the consequence of the curvilinear nature of the mesh, an issue discussed in Ref. 21. The pertinent point here however is that even on this wavy mesh, the higher order interface treatments are stable and recover the single-domain solution. The discrepancy in peak swirl velocity between the single- and the two-domain computation with $F10^{0.4} - 0.0.8.8.8.8$ is less than 1 percent. Figure 7(c) displays contours of the perturbation velocity $\sqrt{(u - u_\infty)^2 + v^2}$ obtained with the $F10^{0.4} - 0.0.8.8.8.8$ filter. The vortex is well-behaved as it moves through the interface. The contour lines are continuous at the noncommunicating overlap point.

2.2.10 Viscous Multidomain Calculations

The experience gained from the previous inviscid cases is now applied to a viscous flow A stringent case is constructed by splitting the domain horizontally, in such a manner that the interface passes through the boundary layer as sketched in Figure 8(a). The implicit time-integration algorithm in the present code mandates a minimum five-point overlap. The compact fully fourth order 44444 difference scheme is coupled with an eighth order

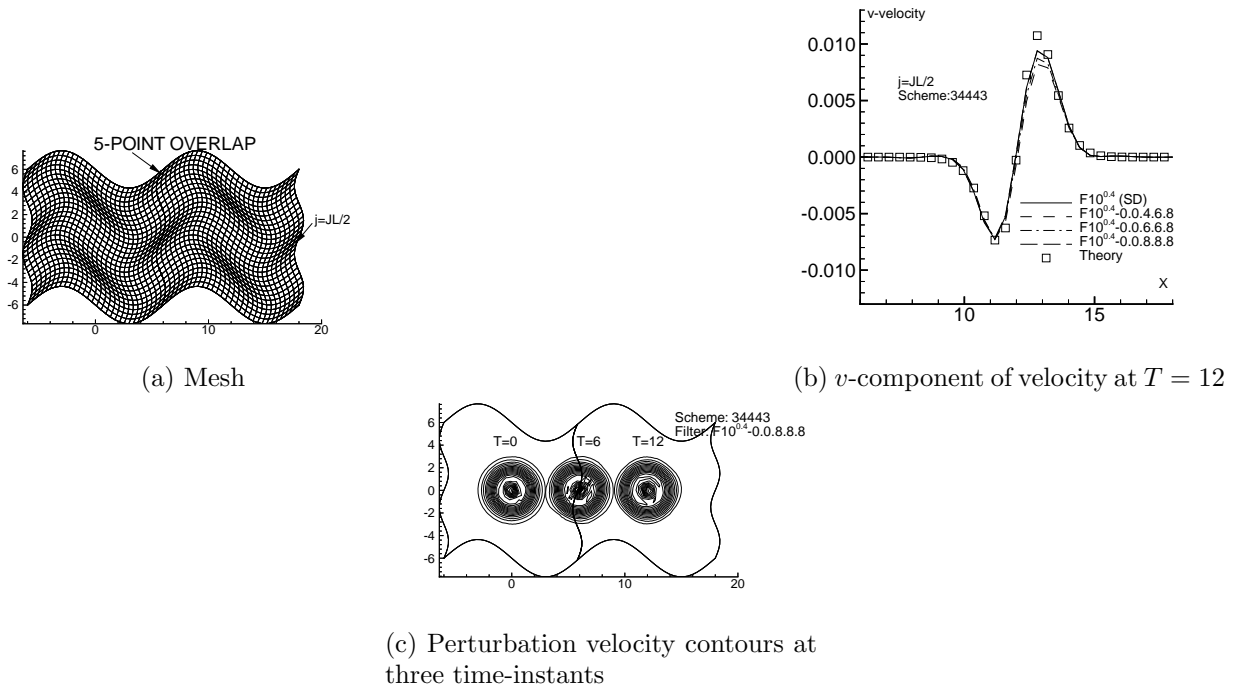


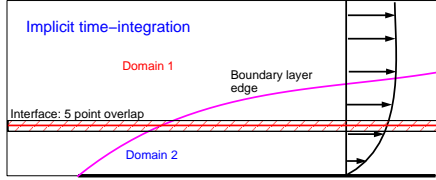
Figure 7: Propagation of Vortex on Multidomain Curvilinear Mesh

interior filter ($\alpha_f = 0.4$). Since the latter requires a 9-point stencil, the lower domain (#1) is chosen to extend a total of 9 points normal to the plate. In this domain, the interior filter formula is applied only at point five since all other points require near-boundary treatment. The noncommunicating overlap point, 7, is located at $y/\delta \sim 0.57$ at the streamwise section corresponding to a Reynolds number of 1.45×10^5 . The outer domain (#2) extends from point five of the original mesh to the outer boundary.

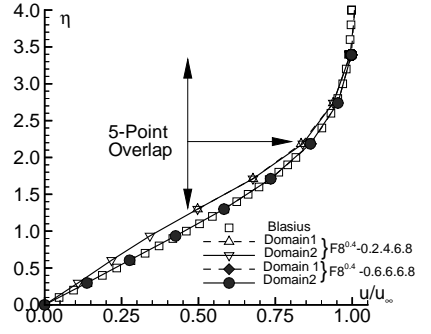
Even on this highly stretched mesh, no numerical instabilities are detected due to the introduction of the interface. The success of the higher order boundary treatment and its superiority over the LOC approach is evident. Close examination reveals that higher order results do not show any significant “drift” in solutions at the NCO. Note that in the LOC results, the $F8^{0.3} - 0 \cdot 2 \cdot 4 \cdot 6 \cdot 8$ filter is employed instead of the more appropriate $F8^{0.3} - 0 \cdot 0 \cdot 4 \cdot 6 \cdot 8$ suggested earlier. This latter choice however is unstable since it leaves point two unfiltered due to present code limitations requiring a “symmetric” choice of filters.

The accuracy and robustness of the boundary filtering formulation is further examined by considering the more practical case of vortex shedding past a circular cylinder. The specific flow conditions are freestream Mach number $M_\infty = 0.1$ and Reynolds number $Re_D = 100$, based on cylinder diameter. A nonorthogonal O-grid of size 155×201 is employed with a nonuniform spatial distribution in both the radial and circumferential directions. All results presented are obtained with the implicit Beam-Warming time-marching algorithm using two sub-iterations and a time step $\Delta t U_\infty / D = 0.002$.

Since this flow field exhibits spatial periodicity in the azimuthal direction, it is first



(a) Schematic



(b) Velocity profiles on mesh FPBL1

Figure 8: Multidomain Flat-Plate Boundary Layer Computation with Five-Point Overlap

computed with a fully periodic formulation of the compact C4 scheme and the eighth order filter, $F8^{0.3}$. Contours of the instantaneous vorticity are shown in Figure 9(a) depicting the Karman vortex street. As previously shown in Ref. 23, these results were found to be in excellent agreement with available highly-resolved computations,²⁷ in terms of Strouhal number and lift/drag coefficients. In order to evaluate the one sided high order filter formulation, the flow was recomputed without invoking the property of spatial periodicity. Instead, a cut was introduced in the azimuthal direction with a five point overlap, as illustrated in the schematic of Figure 9(b). This cut was deliberately placed in the middle of the vortex street to provide a more stringent test of accuracy and stability. Results computed with 44444 and a minimum sixth order filter formulation ($F8^{0.3} - 0.6 \cdot 6 \cdot 6 \cdot 8$) are shown in Figure 9(c). These results are essentially identical to the fully periodic solution of Figure 9(a). By contrast, the LOC method is found to be unstable. Stability (and accuracy) can be recovered by heuristic adjustments of near-boundary values of α_f : in this case, it is necessary to decrease this coefficient at points three and $IL - 2$. This application again demonstrates the superiority and elegance of the one sided, higher order approach since no local adjustment of the filter coefficient is required.

2.3 Applications

The truly multidisciplinary capability of the above algorithm is highlighted with several examples in fluid dynamics, electromagnetics, and magnetogasdynamics. Results pertinent to the requirements of fluid-structure interactions may be found in Ref. 19.

2.4 Fluid Dynamics

The first calculation addresses the unsteady simulation of spiral vortex breakdown above a slender delta wing with a sweep angle of 75° and at 32° angle of attack. The freestream Mach number is 0.2 and the Reynolds number based on centerline chord is 9200. Analysis of this complex phenomenon, which has a significant impact on aircraft control and structural integrity,²⁸ remains a challenge, partly due to the prohibitively large

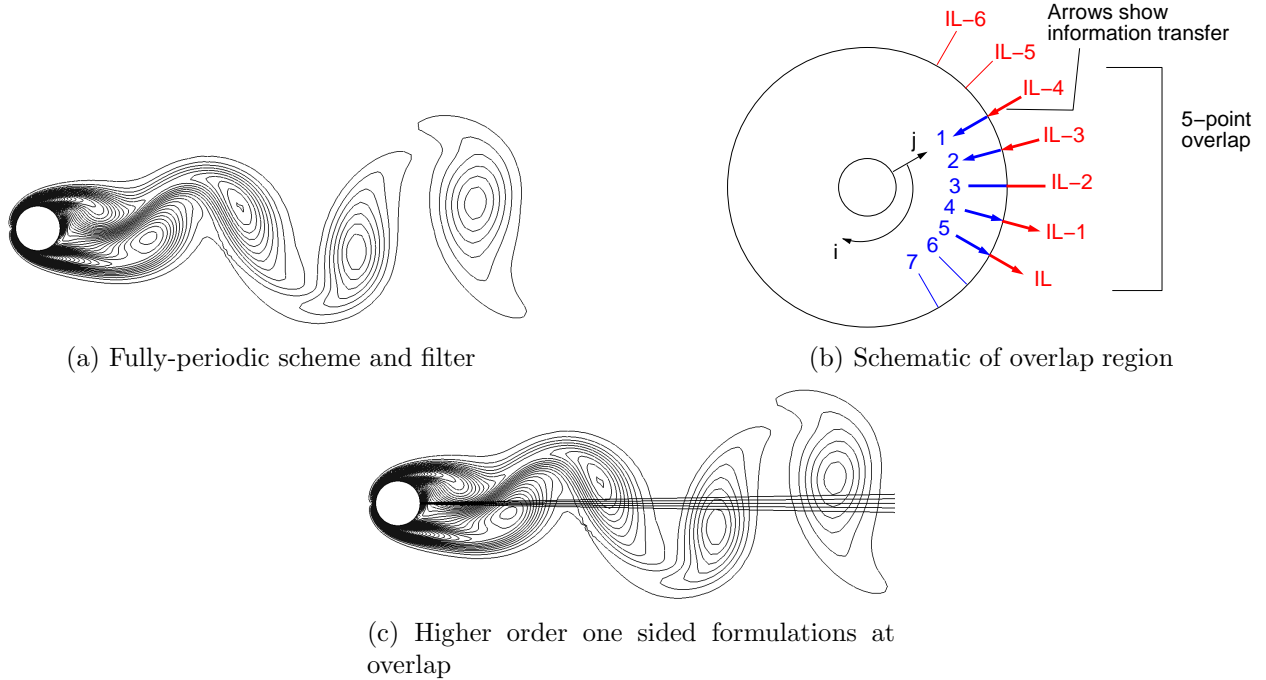


Figure 9: Shedding Past a Cylinder at $Re = 100$

computational resources required for accurate studies. An extensive computational analysis with the E2 scheme, including a mesh resolution study, has been reported in Ref. 28 and is employed to evaluate the accuracy and efficiency gains of the new higher order scheme.

The delta wing is embedded in an H-H topology, highly stretched mesh and represents a challenge in the implementation as well as a test of the robustness of the present scheme. Figures 10 (a), (b) show the instantaneous spanwise-component of vorticity on a vertical plane cutting through the vortex core with E2 for two different grids. Grid 2 contains double the resolution of Grid 1 in the core region and was shown in Ref. 28 to be adequate. At this angle of attack, the breakdown location is highly sensitive to details of the numerical simulation. Thus, on the coarse mesh, the E2 scheme results in a premature breakdown of the vortex. Figure 10 (c) displays results with the C6 scheme supplemented with the tenth order filter on the same mesh. It is observed that the breakdown location is similar to that obtained with E2 on the fine mesh. Whereas Figure 10 (a) shows relatively little detail with only two smeared concentrations of azimuthal vorticity in the vortex wake, the sixth-order scheme C6 with a tenth-order filter, Figure 10 (c), exhibits a much richer structure corresponding to a stronger, tightly wound spiral which is in far better agreement with the grid-converged pattern of Figure 10 (b). An estimate based on these results suggests that the higher order method yields a roughly eight-fold reduction in mesh points and sixteen-fold reduction in computational time.

As another example, the method has been employed to simulate the three-dimensional transition of a forced, finite aspect ratio, plane wall jet.²⁹ The wall jet configuration considered is shown in Figure 11 (a). The main parameters governing the flow are the Reynolds number, the disturbance characteristics at the jet nozzle, the aspect ratio of the channel, and the length of the wall. In the present study, the Reynolds number, based on

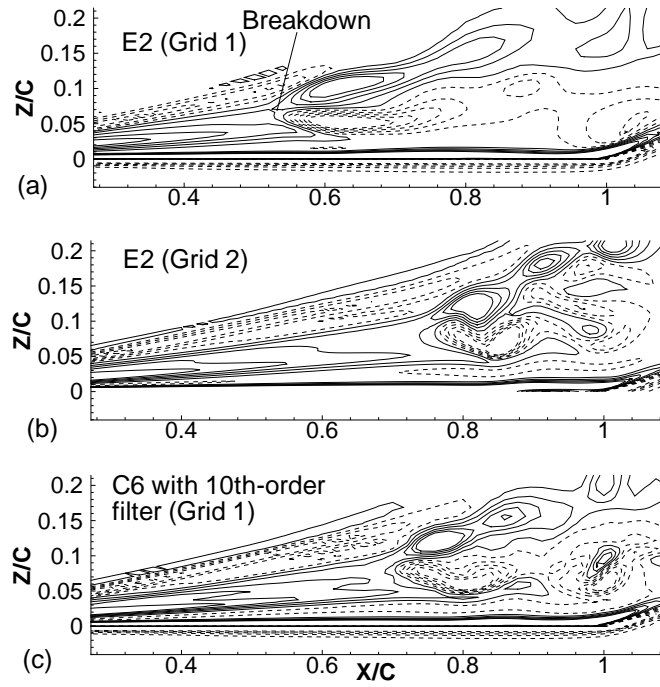
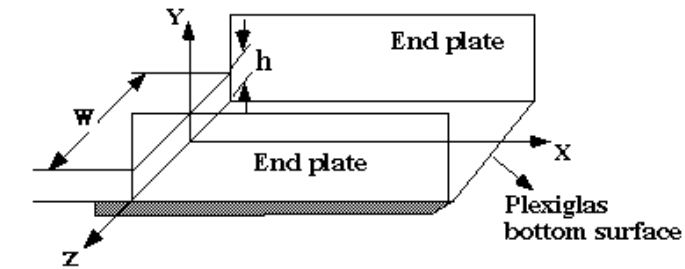
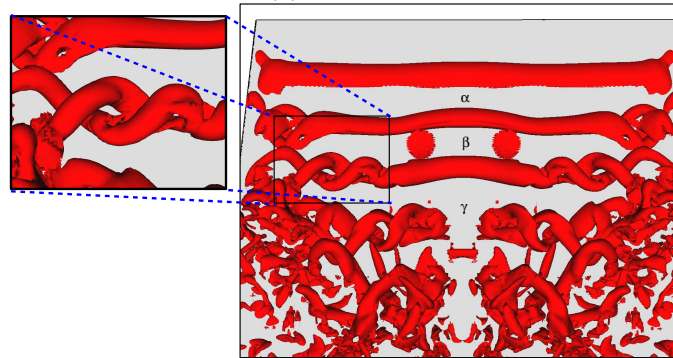


Figure 10: Application to Fluid Dynamics: Vorticity Field in Vortex Breakdown over Delta Wing



(a) Schematic



(b) Isovorticity surface showing double-helical structure

Figure 11: Application to Fluid Dynamics: Simulation of a Forced Transitional Wall-Jet

exit maximum velocity (U_{max}) and nozzle height (h), is 2150. The forcing frequency for this case is $200Hz$ while its amplitude is 6 percent of the maximum centerline velocity. The aspect ratio of the channel is $2b/h = 20$. The mean velocity profile in the normal direction at the nozzle exit is parabolic and corresponds to a fully-developed laminar channel flow in that direction.

An example of the ability of the present high-order scheme to discern the fine-scale breakdown to turbulence is shown in Figure 11 (b) which depicts a 3-D representation of the structure of shear-layer rollers in terms of an iso-surface of vorticity magnitude. The transition process begins with the formation of shear-layer and wall vortex pairs which, due to the energetic forcing, appear close to the nozzle exit and are phased-locked for a short distance downstream. In the course of their spanwise evolution, the rollers are first split into a double-helical structure, which is clearly discernable near the sidewalls. This feature propagates toward the center while also expanding in the radial direction. The spiral branches are wound in a sense opposite to that of the swirl direction of the vortex, consistent with the direction of the induced axial flow which exists within the vortex core. This vortex branching and helical twisting spreads rapidly through self-induction effects, and eventually reaches the symmetry plane where the vorticity magnitude within the vortex core is drastically diminished (hence the apparent break in the iso-surface, region ‘ γ ’ in Figure 11 (b)). Additional details of the simulation and the physics, including impact of forcing parameters and endwall conditions, may be found in Ref. 29.

2.5 Wave Propagation – Electromagnetics

The low dispersion error characteristic of compact-difference schemes is an attractive property in the simulation of wave propagation phenomena associated with acoustic and electromagnetic scattering. In order to demonstrate the capability of the present numerical approach to treat such phenomena, consider the problem of electromagnetic scattering by a sphere of diameter $a = 1$ as an illustrative example demonstrating the capability of the current scheme to solve Maxwell’s equations. The domain of computation is truncated at an outer spherical boundary placed at $r = 2.5$ and is discretized by a spherical $49 \times 49 \times 99$ mesh with uniform variation of dr , $d\theta$ and $d\phi$. The scattered field formulation is employed with a transverse-magnetic (TM) Gaussian pulse for illumination, and the radar cross-section (RCS) is obtained by sampling the response at various frequencies. The bistatic RCS profiles at $ak = 4$ and $ak = 7$, where k is the wave number, are shown in Figure 12 for the $\phi = 0$ longitudinal plane. At these two values of ak , the number of points per wave (PPW) in the radial direction varies from 19 PPW at $ak = 4$ to 11 PPW at $ak = 7$ while the outer boundary placement varies from 2.55λ to 4.46λ respectively. The results are seen to be in very good agreement with the Mie theory and demonstrate considerable advantage over traditional methods which require over 25 PPW for adequate resolution.³⁰

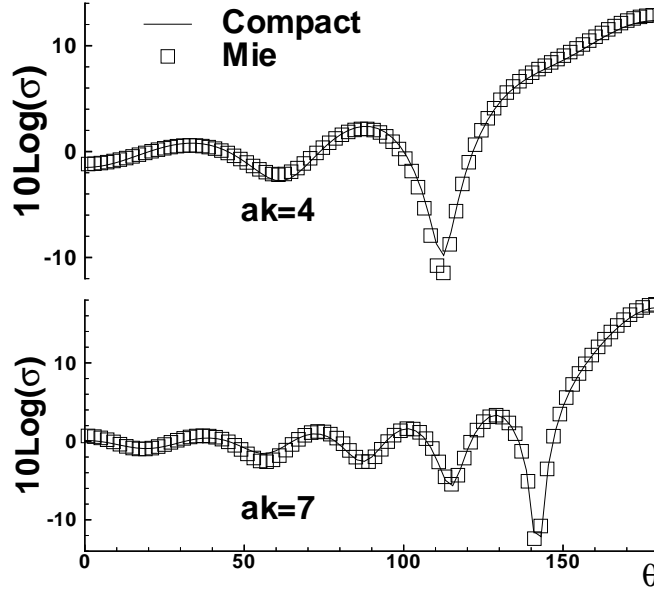


Figure 12: Application to Electromagnetics: Radar Cross Section of a Sphere at $ak = 4.0$ and $ak = 7.0$

2.6 Magnetogasdynamics

There is presently considerable interest in exploring the possibility of utilizing electromagnetic forces to control conducting fluid flow, particularly in the hypersonic regime, to alleviate the stringent environments encountered and to enhance the efficiency of propulsion. From a numerical standpoint, the problem requires careful simulation of the interaction between electromagnetic, pressure and viscous forces described by the magnetogasdynamic equations. The ability of the present scheme to solve these equations has been explored extensively in Refs. 31, 32 and 17. As an example, consider the flow through a channel, depicted in Figure 13 (a) together with a simplified representation of the circuit completing the current path. The pertinent parameter in such flows is the Hartmann number, $Ha = \sqrt{Re Re_\sigma R_b} = B_{ref} L \sqrt{\sigma_{ref} / \mu_{ref}}$ which is a measure of the ratio of magnetic to viscous forces. A uniform magnetic field is imposed in the y -direction ($B_y = 1$) and an electric field, measured by the nondimensional parameter $K = -E_z / (U_{ref} B_{ref})$, is imposed across the channel. If end effects are ignored, the fully developed velocity profile can be obtained by analytic means³³ and can then be employed for validation purposes. The problem is modeled by considering a finite streamwise length of the channel as shown in Figure 13 (b). The traditional zero normal pressure gradient boundary conditions are modified to include the term due to magnetic pressure as described in Ref. 32. Figure 13 (c) exhibits the velocity profile obtained with C4 and the eighth-order filter for $K = 2$ and $Ha = 100$ ($Re = 100$, $R_b = 10$, $Re_\sigma = 10$). The velocity profile without the B field is also shown together with the theoretical result, the equation for which may be found in Ref. 33. Three different meshes are considered consisting of 30×50 , 50×80 and

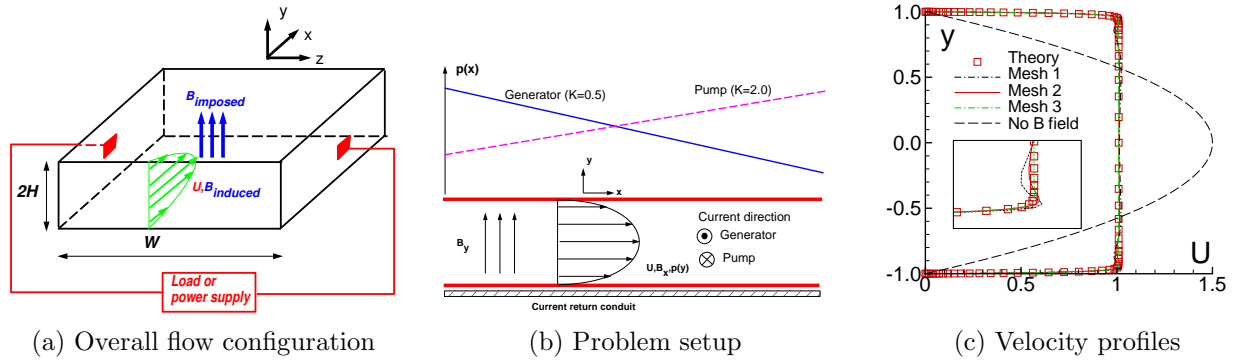


Figure 13: Application to Magnetogasdynamics: Control of Flow in a Channel with Transverse Magnetic Field

50×110 points. The finest mesh contains about 35 points in the Hartmann layers near walls. It is evident that the two coarser meshes exhibit error near the edge of the Hartmann layer (see insert of Figure 13 (c)). In comparison with the case where no B field is applied, the effect of the magnetic field is to flatten the velocity as expected since Lorentz forces diminish shear. Only near the channel walls, where velocity gradients are high, are viscous stresses of the same order as the Maxwell stresses. The computational efficiency advantage from the present higher order method for this case is similar to that reported earlier in the context of vortex breakdown over the delta wing.

3 High-temperature molecular kinetics methodology

The presence of shock waves in high speed flow of an air mixture presents considerable difficulties for accurate numerical simulation of the flowfield. The shock wave redistributes the high kinetic energy of the oncoming flow into various internal energy modes, which relax relatively slowly, leading to significant chemical and thermal nonequilibrium in the stagnation region. In the gas kinetic description, intermolecular collisions change the translational, rotational, vibrational, and electronic energies of the collision partners. The probabilities or effective cross sections of these elementary processes differ significantly, giving rise to widely separate relaxation times for the internal modes. Thus it becomes important to account for the rates of relaxation processes to predict the nonequilibrium behavior of these kinds of flows. Equilibrium is established relatively fast for the translational degree of freedom compared to internal degrees of freedom. The equilibrium Maxwellian distribution is established as a result of the exchange of momentum and kinetic energy among particles. The relaxation time for establishing a Maxwellian distribution in components of air is of the order of the average time between gaskinetic collisions.

$$\tau_{trans} \approx \tau_{gas} = \frac{l}{v} = \frac{1}{Nv\sigma_{gas}}. \quad (22)$$

Here l is the gaskinetic mean free path, v is the average particle velocity, N is the particle number density, and σ_{gas} is the gaskinetic collision cross section. In air at standard conditions, $l \approx 6 \times 10^{-6}$ cm and $\tau_{trans} \approx 10^{-10}$ sec. Usually the gaskinetic times are small in comparison with the flow times over which appreciable changes in the macroscopic parameters of the gas, density or energy, take place. When these conditions are satisfied it is possible to assign at every instant of time a “translational” temperature, which characterizes the average kinetic energy of translational motion of the particles. However, when the velocity distribution function of the particles is anisotropic, as is the case in low density, hypersonic nonequilibrium flows, multiple translational temperatures, one in the direction of flow and the other in the direction perpendicular to the flow, need to be delineated.

For hypersonic flow conditions, besides the nonequilibrium translation, the internal energy modes get excited and it becomes important to model the rotational and vibrational energy relaxation and the coupling of those modes to the dissociation process. The influence of internal energy excitation on dissociation is an area of active research and is addressed in the present report. Early research in dissociation kinetics revealed two divergent theoretical views on the treatment of dissociation. Qualitatively stated, one is the weak bias mechanism³⁴ where dissociation proceeds from the entire vibrational manifold, the dissociation from the low levels driven by rotation. The other is the strong bias mechanism³⁵ based on the assumption that dissociation requires vibrational excitation to within kT of the dissociation limit. Dissociation is a reactive process with an activation energy typically over an order of magnitude greater than the energy associated with V-T exchange. Nonreactive kinetic processes tend to bring about an equilibrium distribution in the vibrational manifold, whereas, the dissociation process perturbs it.³⁶ In the upper quantum energy levels, the vibrational-translational (V-T) kinetic rate processes dominate

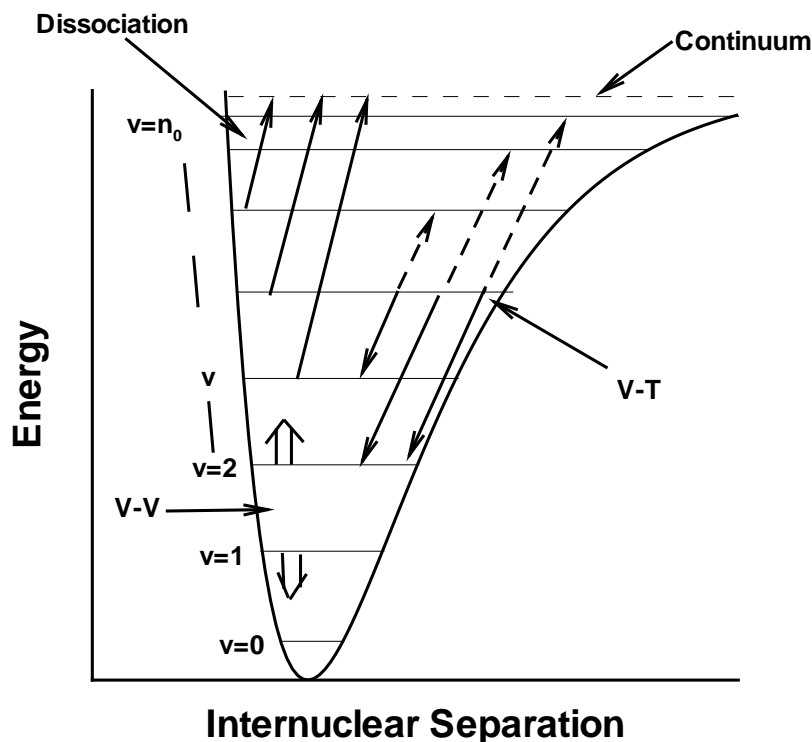


Figure 14: Schematic Showing Multiquantum Transitions in Vibrational States and Dissociation

the energy transfer. In some circumstances, the vibrational-vibrational (V-V) kinetic rate processes can play an important role by accelerating the reaction rates.³⁷ The other issue in the afore-mentioned vibration-dissociation coupling is that of population depletion³⁸ or enhancement³⁹ in the vibrational manifold as a result of the perturbation caused by the dissociation process. A schematic of the vibrational potential well depicting the various processes is shown in Figure 14.

When dissociation takes place, the losses from the vibrational manifold reduce the vibrational populations below the equilibrium values, resulting in a decrease in the dissociation rate. In the work of Josyula and Bailey,⁴⁰ the generalized depletion equations, considering the state-to-state kinetics of dissociating nitrogen, were solved to predict the extent of population depletion in the vibrational manifold. The relative importance of V-V exchanges was quantified for dissociation from last quantum level. However, dissociation can proceed from any quantum level. Recent calculations based on the Forced Harmonic Oscillator (FHO) model suggest that for a small portion of the shock layer behind the blunt body, where the vibrational temperature is less than half the translational temperature, the dissociation proceeds from the low vibrational levels.⁴¹ For the region of the shock wave where the vibrational temperature is nearly equal to the translational temperature, there is only a weak vibrational bias and dissociation proceeds from all the

levels. However, these state-specific predictions have yet to be verified in an experiment. The V-T and V-V transfers can occur by multiquantum energy exchanges in the vibrational manifold. Multiquantum vibrational energy exchanges in highly excited molecules for the CO/CO_2 gas dynamic laser were simulated by several researchers.^{42–45} However, there has been little work on multiquantum energy exchanges for hypersonic air flow past blunt bodies. Multiquantum V-T and V-V transition modeling performed in Ref. 46 using Forced Harmonic Oscillator (FHO) model^{47,48} concluded that dissociation of nitrogen in stagnation regions occurs by multiquantum transitions from the vibrational levels below $v=10$ and not via ladder climbing process.

The present study simulates nonequilibrium relaxation in high speed flows considering multitranslational and rotational temperature modeling. Vibrational relaxation and vibrational-dissociation coupling are examined in the context of a master equation approach under different bias conditions.

3.1 Theoretical Model

The Boltzmann equation expresses the behavior of many-particle kinetic system in terms of the evolution equation for the single particle gas distribution function. The simplified collision model given by the Bhatnagar Gross Krook (BGK) model is formulated as

$$\frac{\partial f}{\partial t} + \mathbf{u} \cdot \frac{\partial f}{\partial \mathbf{x}} = \frac{f^{eq} - f}{\tau}. \quad (23)$$

where f , the distribution function, gives the number density of molecules at position \mathbf{x} and velocity \mathbf{u} at time t . The left hand side of the above equation represents the free streaming of molecules in space, and the right side denotes the collision term. If the distribution function f is known, macroscopic variables of the mass, momentum, energy and stress can be obtained by integration over the moments of molecular velocity. In the BGK model, the collision operator involves a simple relaxation to a local equilibrium distribution function f^{eq} with a characteristic time scale τ . The BGK model was proposed to describe the essential physics of molecular interactions, with τ chosen as the molecular collision time. Based on the above BGK model, the Navier-Stokes equations can be obtained with the Chapman-Enskog expansion truncated to the 1st-order,

$$\begin{aligned} f &= f^{eq} + Knf_1 \\ &= f^{eq} - \tau(\partial f^{eq}/\partial t + \mathbf{u} \cdot \partial f^{eq}/\partial \mathbf{x}). \end{aligned} \quad (24)$$

where, f^{eq} denotes the contribution of the equilibrium part and Knf_1 the nonequilibrium component. With the modification of the particle collision time, the validity of the kinetic model is extended beyond that of the Navier-Stokes equations. An earlier attempt based on this model was successful for shock structure calculations of the monatomic gas with a single translational temperature.⁴⁹

With the above kinetic model, the Navier-Stokes equations in mass-averaged velocity form can be derived,

$$\frac{\partial}{\partial t}(\rho) + \nabla \cdot (\rho \vec{\mathbf{u}}) = 0 \quad (25)$$

$$\frac{\partial}{\partial t}(\rho \bar{\mathbf{u}}) + \nabla \cdot (\rho \bar{\mathbf{u}} \bar{\mathbf{u}} + \bar{\boldsymbol{\sigma}}) = 0. \quad (26)$$

$$\frac{\partial}{\partial t}(\rho e) + \nabla \cdot [\rho e \bar{\mathbf{u}} + \bar{\mathbf{q}} - \bar{\mathbf{u}} \cdot \bar{\boldsymbol{\sigma}}] = 0. \quad (27)$$

Further, to include the internal energy contribution due to the inelastic collisions in the vibrational energy mode, the above mass conservation equation (Eq. 25) can be written to include the source term, $\dot{\omega}_n$,

$$\frac{\partial}{\partial t}(\rho_v) + \nabla \cdot (\rho_v \bar{\mathbf{u}}) = \dot{\omega}_v \quad v=0,1,\dots \quad (28)$$

In the continuum regime, the Navier-Stokes equations could then be used to simulate a flow in thermal disequilibrium. Equations 25 to 27 describe the conservation of mass, momentum and energy in the flowfields of interest. Eqn. 26 and 27 represent the conservation of total momentum and energy, respectively. A microscopic kinetic approach was taken (Eqn. 28) by treating the molecule as anharmonic oscillator, calculating the state populations using the master equation. In the treatment of vibrational energy for the diatomic species in the master equation code, a separate vibrational conservation equation is not necessary as the vibrational energy can be calculated for each quantum level.

The above equations can be derived from the kinetic theory, if the internal energy states at different quantum levels are considered as different species. Modern computational fluid dynamics method consists of solving the continuum equations for updating the total mass, momentum, and energy first through the calculation of the numerical fluxes at each cell interface, the source term given by the vibrational energy master equations, $\frac{\partial}{\partial t}(\rho_v) = \dot{\omega}_v$ can then be updated inside each cell. The advantage of the above continuum formulation (Equations 25 to 27 and Eq. 28) is that nonequilibrium internal energy effects, e.g. those due to the vibrational energy mode, can be described in a detailed manner.

However, the nonequilibrium effects encountered in the transition to the rarefied flows, such as translational and rotational nonequilibrium, cannot be satisfactorily described in the continuum model, hence, a kinetic description, Eq. 23, becomes attractive. In the following section, the modification to Eq. 23 to formulate a multiple translational temperature model is presented.

3.2 Multitranslational Temperature Modeling

For a gas with different translational temperatures in the x, y, and z directions, an anisotropic distribution is assumed with equilibrium state prevailing in a given direction, and for a one dimensional flow, written as:

$$g = \rho \left(\frac{\lambda_x}{\pi}\right)^{1/2} \left(\frac{\lambda_y}{\pi}\right)^{1/2} \left(\frac{\lambda_z}{\pi}\right)^{1/2} \exp[-\lambda_x(u - U)^2 - \lambda_y v^2 - \lambda_z w^2], \quad (29)$$

where ρ is the density, U is the macroscopic velocity in the x -direction, and (u, v, w) the components of the particle velocity in the x, y and z directions, respectively. The

parameter λ is related to the gas temperature, given by $\lambda_x = \mathcal{M}/2kT_x$, $\lambda_y = \mathcal{M}/2kT_y$ and $\lambda_z = \mathcal{M}/2kT_z$. For the multitranslational temperature formulation of a one dimensional flow considered in the present study, we can assume that $T_y = T_z$, such that, $\lambda_y = \lambda_z$. The establishment of the above ellipsoid Maxwell distribution is assumed to be a consequence of particle collisions. Over a long period of time, the above state g will further approach an overall equilibrium state given by \bar{g} ,

$$\bar{g} = \rho \left(\frac{\lambda^{eq}}{\pi} \right)^{3/2} \exp[-\lambda^{eq}((u-U)^2 + v^2 + w^2)]. \quad (30)$$

If the mass, momentum and energy is conserved during the particle collision process, the relationship between an averaged equilibrium temperature T^{eq} ($\lambda^{eq} = \mathcal{M}/2kT^{eq}$) and the individual temperatures T_x, T_y , and T_z is given by,

$$T^{eq} = \frac{1}{3}(T_x + 2T_y), \quad (31)$$

where the assumption $T_y = T_z$ for the one dimensional flow. The above process from g to \bar{g} can be described by the gas-kinetic model

$$g_t + ug_x = (\bar{g} - g)/\tau, \quad (32)$$

which is like the BGK model.⁵⁰ From the above kinetic equation, besides the Navier-Stokes equations for the mass, momentum and total energy, an additional thermal energy equations for the particle random motion in the y and z directions is obtained. For the 1D case, the thermal energy equation becomes

$$(\rho T_y)_t + (\rho U T_y)_x = \frac{\rho R}{3\tau}(T_x - T_y), \quad (33)$$

where R is the gas constant and τ is the particle collision time. The two temperature, continuum Navier-Stokes formulation given by Eq. 32 resembles the hydrodynamical multiple translational temperature equations of Candler et. al.⁵¹ The solutions of the shock structure by solving Eq. 32 using the gas-kinetic scheme⁵² has similar behavior as the results of multitemperature Navier-Stokes results in Ref. 51. The inclusion of two translational temperature as in the above model, results in the shock structure solutions similar to those of Ref. 51 which are thinner with a nonphysical, sharp jump in the calculated density profile inside the shock layer, inconsistent with the DSMC solutions. The discrepancy is more pronounced for the high Mach number cases. Even though the equation was derived from the Boltzmann equation, the model given by Eq. 32 to derive the macroscopic multiple temperature hydrodynamical model in Ref. 51 is intrinsically flawed. Unfortunately, most multitemperature kinetic models in the literature are based on the same assumption of an ellipsoid Maxwellian as in Ref. 51.

In order to improve the previously mentioned kinetic model for the translational nonequilibrium to overcome the erroneous shock solutions, we reconstructed the particle collision process. Starting from the gas distribution function f for a monatomic gas, the particle collisions drive f to g and \bar{g} , instead of from g to \bar{g} alone. During the course of particle collisions, it is difficult to distinguish the process from f to g or from f to \bar{g} . In

terms of the particle collision time for translational nonequilibrium, they can be assumed to be the same. Note, this should not be confused with the nonequilibrium internal energy distribution in a diatomic gas, where the collision time for the rotational relaxation may be much larger than the translational nonequilibrium relaxation. Therefore, for the monatomic gas we construct a generalized BGK model for the translational nonequilibrium,

$$f_t + uf_x = \frac{1}{2} \left[\frac{g - f}{\tau} + \frac{\bar{g} - f}{\tau} \right], \quad (34)$$

where f is the real gas distribution function, and g and \bar{g} are the corresponding Maxwellians. Note that the particle collision time τ is related to the local dynamical viscosity μ and pressure p , i.e., $\tau = \mu/p$. The relation between mass ρ , momentum ρU , total energy ρE , and the thermal energy ρE_{y-z} in the y and z directions are

$$W = \begin{pmatrix} \rho \\ \rho U \\ \rho E \\ \rho E_{y-z} \end{pmatrix} = \int \boldsymbol{\psi} f dud\xi d\eta, \quad (35)$$

where $\boldsymbol{\psi}$ has the components

$$\boldsymbol{\psi} = (1, u, \frac{1}{2}(u^2 + v^2 + w^2), \frac{1}{2}(v^2 + w^2))^T. \quad (36)$$

Since only mass, momentum and total energy are conserved during particle collisions, f and g satisfy the condition

$$\int \frac{1}{2} [(g - f) + (\bar{g} - f)] \psi_\alpha dudvdw = S = (0, 0, 0, s)^T, \quad \alpha = 1, 2, 3, 4. \quad (37)$$

The source term s can be still be modeled as $s = \rho R(T_x - T_y)/3\tau$.

For any kinetic model for multiple translational temperature nonequilibrium, one basic requirement is that the averaged temperature $T^{eq} = \frac{1}{3}(T_x + 2T_y)$ in the 1D case should be the same temperature as the one temperature gas kinetic model. If we take moments $(u - U)^2$, v^2 and w^2 on the model given by Eq. 34, we can obtain the temperature evolution equations for individual direction. When we add them together and use the condition $3T = T_x + T_y + T_z$, a single equation for the averaged temperature T can be obtained,

$$(\rho T)_t + (\rho UT)_x = (\rho T^{eq} - \rho T)/\tau,$$

which is the same temperature evolution equation from a single temperature BGK model, i.e. $f_t + uf_x = (\bar{g} - f)/\tau$. So, the averaged temperature from the two-temperature kinetic model, Eq. 34, is the same as that from a single temperature model. The model given by Eq. 34 is, thus, shown to be a valid extension to recover the multiple temperature nonequilibrium from the original BGK model.

In order to test the above model (Eq. 34), the numerical method developed in Ref. 52 is used to solve Eq. 34. For a finite volume method,

$$W_j^{n+1} = W_j^n + \frac{1}{\Delta x} \int_0^{\Delta t} (F_{j-1/2}(t) - F_{j+1/2}(t)) dt + S_j^n \Delta t, \quad (38)$$

where W_j^n is the cell averaged mass, momentum, total energy, and the thermal energy in y and z directions, and $F_{j+1/2}$ is the corresponding fluxes at a cell interface by solving Eq. 34. Note that Δt is the time step $\Delta t = t^{n+1} - t^n$, and S_j^n is the source term for the thermal energy. The evaluation of the fluxes is based on the gas distribution function f at a cell interface. For the shock structure calculation, due to the smoothness inside the shock layer, the gas distribution function at a cell interface is constructed using the Chapman-Enskog expansion and has the form

$$f = \frac{1}{2}(g + \bar{g}) - \frac{1}{2}\tau[g_t + \bar{g}_t + u(g_x + \bar{g}_x)] + \frac{1}{2}t(g_t + \bar{g}_t) \quad (39)$$

where the g_x and \bar{g}_x can be obtained from the gradients of macroscopic variables, and g_t and \bar{g}_t can be evaluated from the compatibility conditions

$$\int (g_t + ug_x)\psi_\alpha dudvdw = 0 \quad \text{and} \quad \int (\bar{g}_t + u\bar{g}_x)dudvdw = 0.$$

For more details, see Ref. 52. Even with the ability to recover two translational temperatures, the nonequilibrium distribution (Eq. 39) is truncated to the Navier-Stokes order and it will not be accurate in the description of rarefied flow. The anomalous density jump given by the model of Eq. 32(found in Ref. 51) does not appear in the solutions given by the present formulation. However, the shock thickness is still thinner in comparison with experimental measurements and the DSMC solutions. Theoretically, it seems that we should continue this expansion in Eq. 39 to go to Burnett and Super-Burnett orders. Unfortunately, the success from the higher order expansion is limited, and there is no evidence that the successive expansions converge. Additionally, we can replace the collision time τ in Eq.(39) with a generalized one, τ_* , and assume that there is a closed form solution of the BGK model. We can obtain a relation between τ_* and τ . In the current study, the new collision model (Eq. 34) is used with BGK-Xu method⁴⁹ to establish a generalized particle collision time τ_* ,

$$\tau_* = \tau / (1 + \tau \langle D^2 g \rangle / \langle Dg \rangle) \quad (40)$$

where $D = \partial_t + u\partial_x$ and $\langle \dots \rangle = \int (\dots)(u - U)^2 dudvdw$. Here τ depends on the macroscopic variables through the relation $\tau p = \mu_\infty (T/T_\infty)^\omega$, and the generalized τ^* will depend not only on the macroscopic variables, but also on their gradients. Therefore, the evaluation of τ^* represents a set of generalized constitutive relations for the calculation of the translational nonequilibrium flow. In order to simulate the flow with a realistic Prandtl number, a modification of the heat flux in the energy transport at a cell interface, as used in Ref. 52, is implemented in the current study.

3.3 Rotational Temperature Modeling

The model given by Eq. 34 can be extended to the rotational nonequilibrium as well. As shown above, the average temperature of the multiple translational model is the same as the temperature for one translational temperature model. Therefore, we will use a single

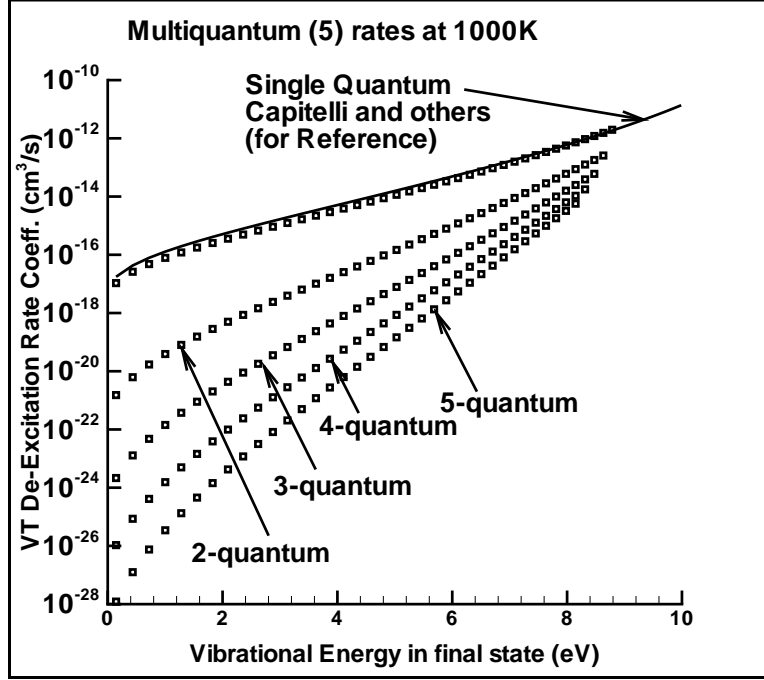


Figure 15: Multiquantum V-T Transition Rates for five Quantum Levels at 1000 K for the N_2 Molecule

temperature for the translational degree of freedom in what follows. With the inclusion of rotational degree of freedom, the equilibrium state can be written as

$$g = \rho \left(\frac{\lambda_t}{\pi} \right)^{3/2} \left(\frac{\lambda_r}{\pi} \right) \exp[-\lambda_t((u - U)^2 + v^2 + w^2) - \lambda_r \xi^2]. \quad (41)$$

Due to the particle collisions, the above ellipsoid distribution will approach equilibrium,

$$\bar{g} = \rho \left(\frac{\lambda^{eq}}{\pi} \right)^{5/2} \exp[-\lambda^{eq}((u - U)^2 + v^2 + w^2 + \xi^2)]. \quad (42)$$

Similar to the model given by Eq. 34, we can construct a kinetic model for translational and rotational nonequilibrium,

$$f_t + u f_x = \frac{1}{2} \left[\frac{g - f}{\tau_t} + \frac{\bar{g} - f}{\tau_r} \right], \quad (43)$$

where, due to the different time scales of translational and rotational modes to achieve the equilibrium state, two different collision times τ_t and τ_r are used in the present study for the condition $\tau_r \gg \tau_t$. The relationship of $\tau_r = Z_r \tau_t$ was invoked, with the value of Z_r ranging⁵³ between three and five for the flows considered in the present study.

The distribution function f can approach g rapidly, then slowly from g to \bar{g} . Thus, the above model Eq. 43 can be further simplified as shown below to calculate the numerical fluxes,

$$f_t + u f_x = (g - f)/\tau_t, \quad (44)$$

where the fast transition part is captured in the above model. For the rotational nonequilibrium flow, a finite volume scheme similar to Eq. 38 was used with the numerical fluxes based on the above simplified model Eq. 44.

3.4 Multiquantum Energy Exchanges in the Vibrational Manifold

The conservation Eqn. 28 is written for the mass density in quantum level v . The source term $\dot{\omega}_v$ derived from the vibrational master equations includes the relevant energy exchange processes consisting of the V-T, V-V and dissociation. The mass density of the molecular species is the sum of the corresponding state densities in the vibrational levels.

$$\rho = \sum_{v=0}^{v_{last}} \rho_v \quad (45)$$

The symbolic equations governing the V-T transitions responsible for the variation of the particles distributed in the v^{th} vibrational level are:

$$N_2(v) + N_2 \Omega N_2(v') + N_2 \quad (46)$$

the equations governing the V-V process are:

$$N_2(v) + N_2(w) \Omega N_2(v') + N_2(w') \quad (47)$$

and the equations governing the dissociation process for the Ladder model shown here for reference (the following section presents the weak bias model as well):

$$N_2(v_{last}) + N_2 \rightarrow 2N + N_2 \quad (48)$$

The kinetics of the particle exchanges among the quantum states are simulated using the vibrational master equation, the population distributions are calculated with:⁵⁴

$$\dot{\omega}_v = \frac{1}{\mathcal{M}} \left\{ \sum_{v'} [k_{VT}(v' \rightarrow v) \rho_{v'} \rho - k_{VT}(v \rightarrow v') \rho_v \rho] + \sum_{w, v', w'} [r_{VV}(v', w' \rightarrow v, w) \rho_{v'} \rho_{w'} - r_{VV}(v, w \rightarrow v', w') \rho_v \rho_w] \right\} \quad (49)$$

The V-T process is associated with the rate coefficient k_{VT} where the molecule loses or gains a vibrational quantum. The de-excitation rate from v' to v is denoted by $k_{VT}(v' \rightarrow v)$, the inverse collision from $v \rightarrow v'$ by $k_{VT}(v \rightarrow v')$. The multiquantum transition rates are from the work of Adamovich, et al.⁴⁸ shown in Figure 15, and 16, are for 1,000 K (5 quantum) and 10,000 K (5 quantum). At 1,000 K, the single quantum V-T transition rates of Capitelli, et al. match, whereas, at 10,000 K the Capitelli, et al. rates are higher than the FHO rates, with the maximum difference an order of magnitude for the last level. On the other hand, when considering V-V exchanges, the initial and final vibrational states of each collision partner must be identified; thus the transition rate from

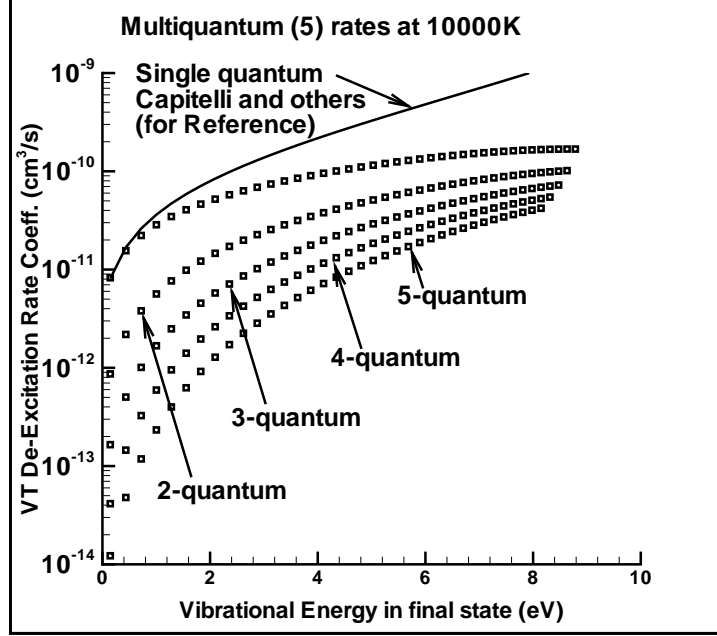


Figure 16: Multiquantum V-T Transition Rates for Five Quantum Levels at 10000K for the N_2 Molecule

v' to v and w' to w is given by $r_{VV}(v', w' \rightarrow v, w)$. Consistency of the rate coefficient with the principle of detailed balance is enforced. Single quantum V-V transfer rates implemented in the present study were taken from Doroshenko, et al.⁵⁵

The vibrational energy of the diatomic molecules, treated as anharmonic oscillators, is given by,

$$e_{vib} = \sum_{v=0}^{v_0} \frac{\rho_v}{\rho} \epsilon_v \quad (50)$$

where the index v enumerates the vibrational quantum level. In this equation, ρ_v/ρ is the fractional population of the v^{th} vibrational level and ϵ_v the quantum level energy given by the third-order approximating formula:

$$\frac{\epsilon_v}{hc} = \omega_e(v + \frac{1}{2}) - \omega_e x_e(v + \frac{1}{2})^2 + \omega_e y_e(v + \frac{1}{2})^3 \quad v=0,1,2,\dots,v_0 \quad (51)$$

where h is the Planck's constant and c is the speed of light. Here, ϵ_1 denotes ground state vibrational energy, ϵ_2 denotes first excited state, and so on. The spectroscopic constants are given by,⁵⁶ $\omega_e=2358.57 \text{ cm}^{-1}$, $\omega_e x_e=14.324 \text{ cm}^{-1}$, and $\omega_e y_e=-0.00226 \text{ cm}^{-1}$. When $v_0=47$, the value of energy exceeds the N_2 dissociation energy, 9.86 eV.

3.5 Vibrational Bias and Depletion in Dissociation

With an increase in flow temperatures, an accumulation of internal energy leads to dissociation of the diatomic molecules. The dissociation process in the continuum

formulation is modeled in the form of an Arrhenius equation

$$k_f(T_{\text{eff}}) = C_f T_{\text{eff}}^\eta \exp(\theta_d/T_{\text{eff}}) \quad (52)$$

where the rate controlling temperature, T_{eff} requires an appropriate definition. Present day hypersonic codes have often used the Park model to define the rate controlling dissociation temperature, due to its ease of implementation. However, the model has been shown to be inaccurate for a wide range of temperatures. In order to highlight the kinetic implications of nonequilibrium relaxation, dissociation models differing in the vibrational bias, suitable for a wide range of degrees of nonequilibrium are discussed. The present study examines the behavior of these continuum dissociation models in oxygen and nitrogen baths maintained at a gas temperature of 6,000 K and 10,000 K, respectively for the vibrational temperature ranging between 2,000 and 12,500 K. Brief description of the dissociation models follows.

The Park model⁵⁷ expresses the dissociation coefficient in terms of an effective temperature:

$$T_{\text{eff}} = \sqrt{TT_v} \quad (53)$$

$$k_{d,\text{eff}} = k_{d,\text{eq}}(T_{\text{eff}}) \quad (54)$$

The ladder and weak bias model were developed considering the energy in the vibrational quantum states of the dissociating diatomic molecule. Dissociation in the ladder model is assumed to take place only from the last bound state whereas for the weak bias model *all* quantum states contribute. The dissociation rate of the Ladder model can be written as,

$$n_v^* k_{v^* \rightarrow \text{Continuum}} \quad (55)$$

where, n_v^* is the vibrational population in the last state and $k_{v^* \rightarrow \text{Continuum}}$ is the dissociation rate from the last vibrational state.

The weak bias model, in contrast to the previous model, assumes dissociation to proceed from all the states, viz. $n_0 k_{0 \rightarrow \text{Continuum}}$, $n_1 k_{1 \rightarrow \text{Continuum}}$, $n_2 k_{2 \rightarrow \text{Continuum}}$ and so on to $n_v^* k_{v^* \rightarrow \text{Continuum}}$.

In order to facilitate a comparison of the global rate of dissociation under different conditions of vibrational bias, it is useful to define an effective dissociation rate, $k_{d,\text{eff}}[T, T_v]$, where:

$$k_{d,\text{eff}}[T, T_v] N_{\text{tot}} \equiv \sum_{v=0}^{v^*} k_{d_v} n_v \quad (56)$$

and k_{d_v} is the dissociation coefficient from vibrational state v and is assumed to be a function of T only. By expressing the functional dependence of the population in each vibrational state in terms of a vibrational temperature:

$$n_v = \frac{N_{\text{tot}} \exp\left(\frac{-\epsilon_v}{kT_v}\right)}{Z_{\text{vib}}} \quad (57)$$

where Z_{vib} is the vibrational partition function, ϵ_v is the vibrational energy in the quantum level v , k is the Boltzmann constant, N_{tot} is the total number density, and T_v is the

vibrational temperature, one can express the $k_{d\text{eff}}[T, T_v]$ for the ladder and weak bias model in terms of the equilibrium coefficient $k_{d\text{eq}}[T]$. In equilibrium,

$$k_{d\text{eq}}[T] = \sum_{v=0}^{v^*} k_{d_v} \frac{n_{v\text{eq}}}{N_{\text{tot}}} = \sum_{v=0}^{v^*} k_{d_v} \frac{\exp[-\epsilon_v/kT]}{Z_{\text{vib}}[T]} \quad (58)$$

For the Ladder model,

$$k_{d\text{eff}}[T, T_v] = k_{d_{v^*}} \frac{n_{v^*}}{N_{\text{tot}}} = k_{d\text{eq}}[T] \frac{n_{v^*}}{n_{v\text{eq}}} = k_{d\text{eq}}[T] \exp[\epsilon_v(\frac{1}{T} - \frac{1}{T_v})] \frac{Z_{\text{vib}}[T]}{Z_{\text{vib}}[T_v]} \quad (59)$$

A simple weak bias model may be constructed by assuming:

$$k_{d_v} = k_0[T] \exp[-(D - \epsilon_v)/T] \quad (60)$$

where, the value of k_0 is established by requiring consistency with the equilibrium rate coefficient:

$$k_0[T] = Z_{\text{vib}}[T] k_{d\text{eq}}[T] \frac{\exp(D/kT)}{(v^* + 1)} \quad (61)$$

Substitution for k_{d_v} yields for this weak bias form:

$$k_{d\text{eff}}[T, T_v] = \frac{k_{d\text{eq}}[T]}{(v^* + 1)} \frac{Z_{\text{vib}}[T]}{Z_{\text{vib}}[T_v]} N_{\text{tot}} \sum_{v=0}^{v^*} \exp[\epsilon_v(\frac{1}{T} - \frac{1}{T_v})] \quad (62)$$

Note that nonequilibrium values of the effective dissociation coefficient for the ladder and weak bias forms differ substantially. The state-specific dissociation rates compete with the V-V and V-T rates and the state populations are depleted in the excitation phase.

The above-mentioned Ladder model does not account for depletion of the vibrational population. In the present study, the Ladder model with the effect of population depletion was also implemented. The vibrational population depletion on account of energy loss of dissociation was modeled according to the approach outlined by Osipov and Stupochenko.³⁶ This model was developed by Josyula and Bailey in Refs. 38 and 40, the study accounted for effects of V-T and V-V transition rates. An analytic expression of the resulting reduction in the equilibrium dissociation rate was derived by defining φ_v to give the deviation of the quasi-steady distribution from an equilibrium Boltzmann distribution. The mass density in vibrational state v is:

$$\rho_v(t) = \rho_v^{(0)}(1 + \varphi_v) \quad (63)$$

The deviation of the population of level v from equilibrium is given by φ_v which relates ρ_v (the state mass density in level v) to $\rho_v^{(0)}$ (the state mass density in level v at equilibrium). It is seen from Eq. 63 that when $\varphi_v < 0$, the level population *decreases* relative to the equilibrium population.

The coupled conservation equations used the Roe approximate Riemann solver, implemented in finite volume formulation by computing the cell interface flux as a summation of wave speeds, similar to Eq. 38. The second order spatial accuracy was obtained by employing the MUSCL approach in conjunction with the minmod limiter to reduce the solution to first order accuracy in the vicinity of strong shock waves, as described in the work of Josyula, et al.⁵⁴ An explicit predictor-corrector method is used to advance the solution in time.

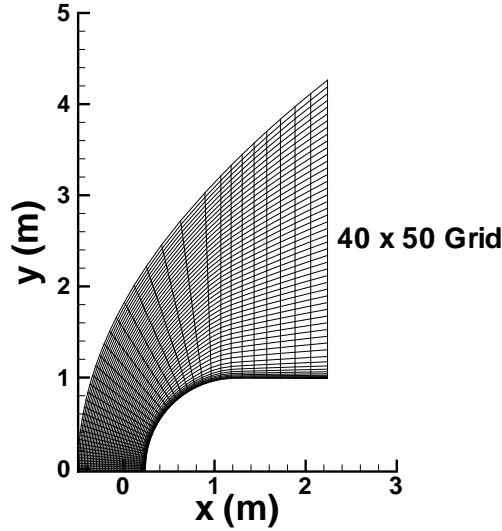


Figure 17: Typical Computational Grid for Blunt Body Flow

3.6 Results and Discussion

Results are presented in three sections. In the first section, the multitranslational temperature comparisons with DSMC solutions of the shock structure in translational and rotational nonequilibrium for Mach 1.2 to 5.0 shock waves will be presented. This will be followed by the flow simulations past two-dimensional blunt bodies for Mach numbers from 6.5 to 19.83 to assess the effect of multiquantum V-T energy exchanges on the relaxation process and the effect of vibrational bias in the dissociation process. A typical computational grid used for the solution of the axisymmetric blunt body flows in thermal and chemical nonequilibrium is shown in Figure 17.

3.7 Multitranslational and Rotational Temperatures in Shock Structure

To determine the predictive accuracy of the multitranslational temperature model, the internal structure of a shock wave was simulated. Since there are no experimental data for the two-translational temperature measurements, the present calculation will be compared with the DSMC solutions. Currently, the DSMC is the most reliable method to obtain solutions of a shock structure that is in thermodynamic nonequilibrium. The present calculations use a monatomic gas with the atomic weight of argon and a Maxwellian (inverse fourth power) inter-atomic potential ($\mu_{ref} = 2.515 \times 10^{-5} kg/ms$, $T_{ref} = 273K$, and $\omega = 1$). All cases use an equal space mesh of 200 grid points. Candler et. al.⁵¹ conducted a study of shock structure with multiple translational temperatures using a continuum method and compared with DSMC results. The continuum study of Ref. 51 predicted a much thinner shock width than that of DSMC predictions. The solutions of the present

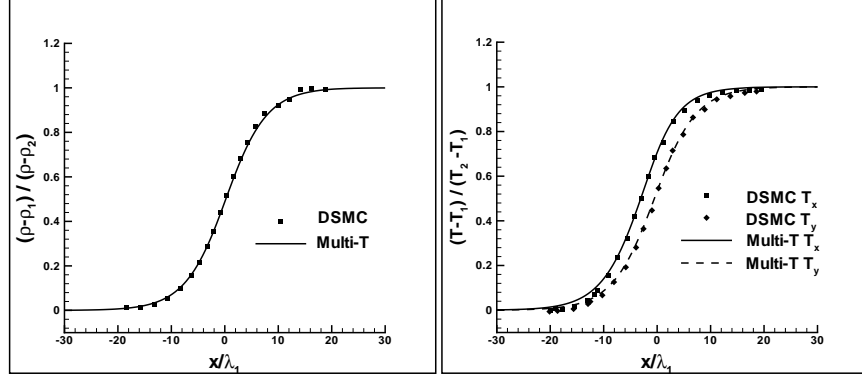


Figure 18: Computed Normalized Density and Temperatures for a Mach 1.2 Maxwellian Gas Shock Wave

study will be compared with the DSMC shock structure predictions presented in Ref. 51. Figures 18 through 20 plot the Maxwellian gas shock waves for free-stream Mach numbers between 1.2 to 5.0.

The normalized temperature, $T_n = (T - T_1)/(T_2 - T_1)$, and normalized density $\rho_n = (\rho - \rho_1)/(\rho_2 - \rho_1)$ are plotted versus x/λ_1 . The upstream mean-free paths λ_1 is defined as $\lambda_1 = 2\mu/\rho_1\bar{C}_1$, where \bar{C}_1 is the mean atomic speed at the upstream conditions. The temperature is resolved in the components perpendicular (x direction) and parallel (y direction) to the shock wave. From these figures, we can see the excellent match between the current results and DSMC solutions for all Mach number cases from the continuum ($M = 1.2$) to the highly nonequilibrium one ($M = 5$). For the Mach 5 flow, there is slight disagreement with the DSMC solution in the upstream location. The density and rotational temperature have also been compared with the experimental data of Robben and Talbot.⁵⁸ The computation considered a pre-shock temperature of 9.15 K. The measured rotational temperature and density have been observed to be accurately predicted by the present continuum model.

3.8 Effect of MultiQuantum V-T Exchanges on Vibrational Temperatures in Blunt Body Flows

The flow conditions for the results shown in the Figures 21 and 22 are: $M_\infty=6.5$, $p_\infty=50$ Pa and $T_\infty=300$ K, for pure nitrogen flow past an infinite cylinder of 1 meter radius. Figure 21 shows temperature distributions in the flowfield for computations assuming single, double and six-quantum V-T energy exchanges, with and without single quantum V-V energy exchanges; Figure 21a along the stagnation streamline and Figure 21b along the surface. An anharmonic oscillator with 40 quantum levels for the nitrogen molecule was assumed and the thermal nonequilibrium contribution was coupled to the fluid dynamics equations. The results indicate that the influence of multiquantum V-T

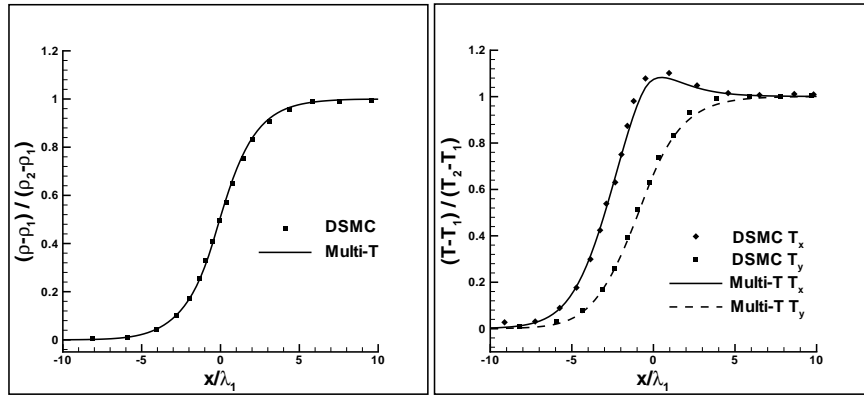


Figure 19: Computed Normalized Density and Temperatures for a Mach 2.0 Maxwellian Gas Shock Wave

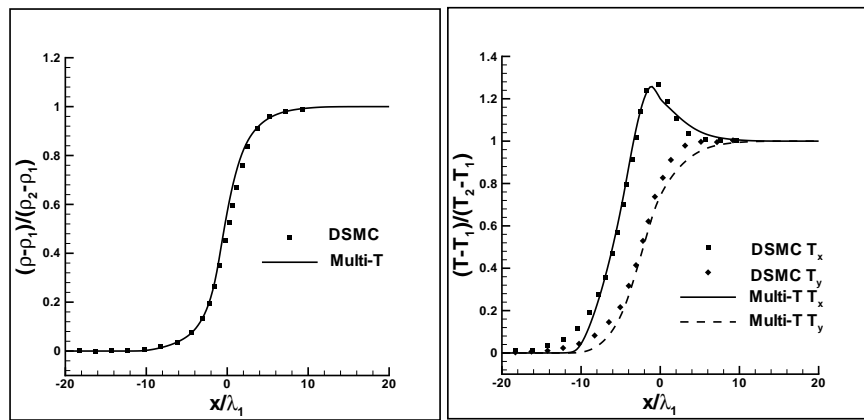


Figure 20: Computed Normalized Density and Temperatures for a Mach 5.0 Maxwellian Gas Shock Wave

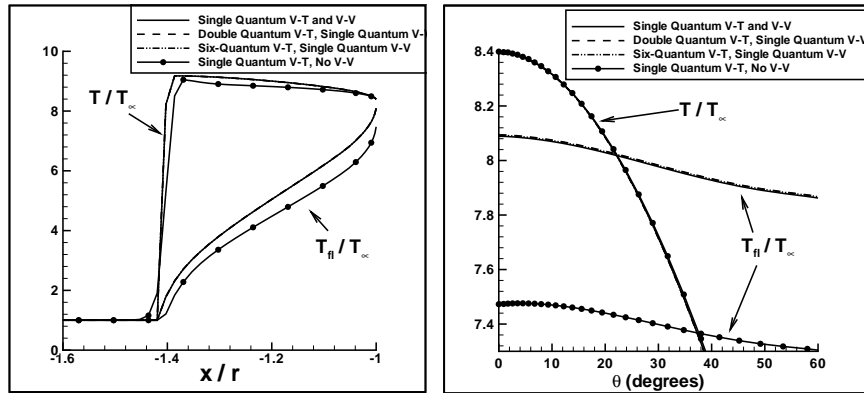


Figure 21: Comparison of Temperatures Along Stagnation Streamline and Along Surface for Nitrogen Flow Past Blunt Body

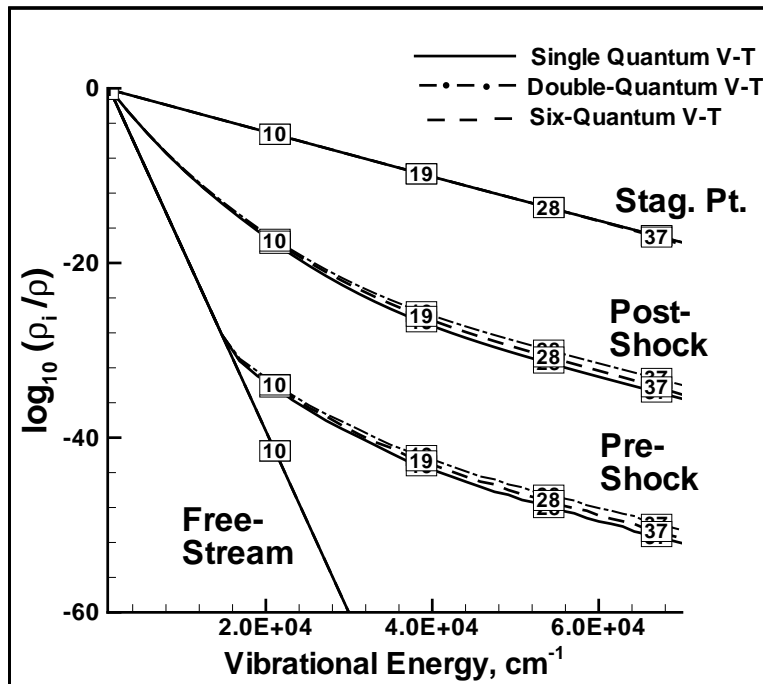


Figure 22: Population Distribution at Select Locations Along Stagnation Streamline for Nitrogen Flow Past Blunt Body

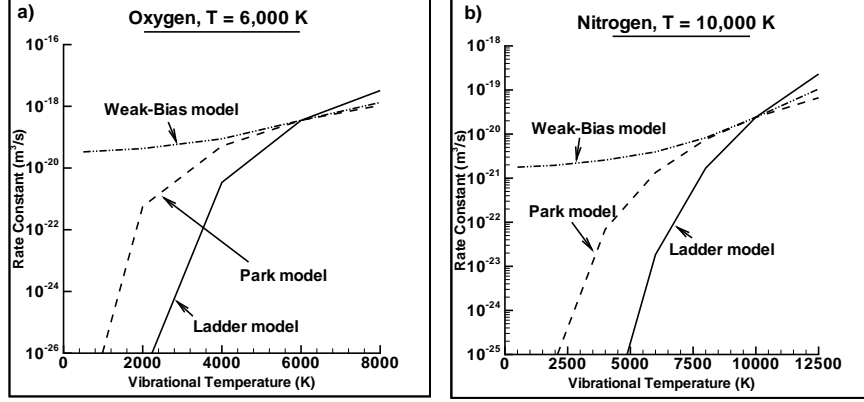


Figure 23: Comparison of Vibrational Biases on the Effective Dissociation Rate Coefficient

transitions on the translational and first-level vibrational temperatures along the stagnation streamline and surface are negligible. The results show a small influence of the inclusion of single quantum V-V exchanges on the translational temperature along the stagnation streamline, V-V energy transfers speed up the relaxation process. There is, however, a more pronounced effect of V-V exchanges on the first level vibrational temperature. Figure 22 shows the population distribution for nitrogen along the stagnation streamline at the freestream, pre-shock, post-shock and stagnation point locations. The negligible influence of multiquantum transitions are also seen in these results. At the lower Mach number of 6.5 considered in the present study, it may be concluded that multiquantum V-T exchanges have a minor effect on the vibrational relaxation process.

3.9 Effect of Vibrational Bias in Blunt Body Flows

Figure 23 shows the calculated two-temperature dissociation rate constant $k_{d, \text{eff}}(T, T_v)$ for the cases of oxygen and nitrogen baths maintained at $T = 6,000$ K and $T = 10,000$ K, respectively. The vibrational temperature varies from 500 K to 12,500 K. This represents the basic condition that arises in shock layer compression flows, where the internal mode temperature lags that of translational temperature. The comparison of different biases of the dissociation mechanism reveals large differences at vibrational temperatures far from equilibrium. From previous studies (See for example Ref. 41) it is conjectured that for T_v/T less than 0.5, the dissociation occurs from the lower levels and for $T_v \sim T$, dissociation can occur from all the levels. The figure shows, for $T > T_v$, the rate coefficients of the Ladder model (signifying strong bias) are several orders of magnitude lower than those of the weak bias model. For $T < T_v$, the trend is reversed and the Ladder model has a higher rate coefficient than the weak bias model. The results from the Park model are shown for reference. It may be concluded that the stronger the bias, the more rapid is the decrease in the rate coefficient for $T_v < T$.

Figure 24 shows the inverse of the term in Equation (63), $1 + \varphi_l$ which gives the dissociation reduction factor from Park's equilibrium rates plotted as a function of

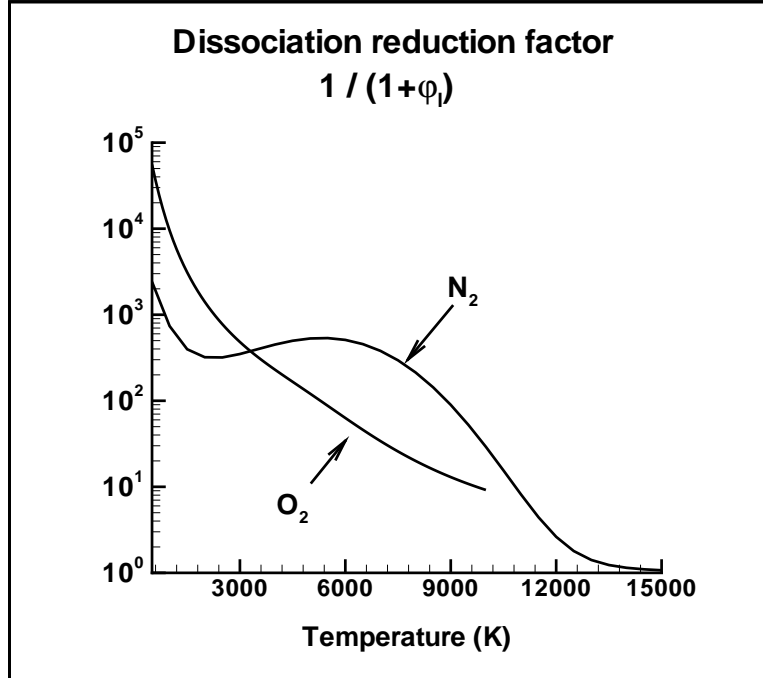


Figure 24: Dissociation Reduction Factor for Oxygen and Nitrogen Due to Depletion

temperature. Note that when $\varphi_l < 0$, the effect is to deplete the population in the vibrational states. The reduction factor, $\frac{1}{1+\varphi_l}$, is the ratio of the level population distribution at equilibrium to the nonequilibrium state. The reduction factor which accounts for the deviation from the quasi-steady state distribution can range from 1 to 3 orders of magnitude between the temperatures of 5,000 K to 10,000 K at which there is considerable nitrogen dissociation. This factor was applied as a correction to the Park's dissociation rates to account for the depletion effects in the vibrational levels. It is important to note that the reduction factor is the highest below 2,000 K but there is negligible nitrogen dissociation at this temperature. The reduction factor again peaks at about 6,000 K and stays high till 12,000 K, a region of significant nitrogen dissociation and at higher temperatures begins to fall and reaches a factor of 1 at the highest temperature of 15,000 K. The dissociation reduction factor in oxygen dissociation also shown in Figure 24 up to a temperature of 10,000 K shows a similar trend as for nitrogen.

Figure 25 shows the effect of the various dissociation models including the ladder model with depletion effects on stagnation streamline profiles for a Mach 19.83 nitrogen flow past a blunt body. The Park dissociation model captures qualitatively, [Figure 25(a)], the expected nonequilibrium between the translational and vibrational modes. Shown here are the temperature profiles with depletion effects; the large depletion (see Figure 24 for dissociation reduction factor), reduces the effective dissociation rate, thereby, increasing the shock-standoff distance. Figure 25(b) compares profiles of atomic nitrogen production for the various models. Note the extended region of near-equilibrium conditions prevailing in the shock layer for this strong shock case. The Ladder model with depletion differs from

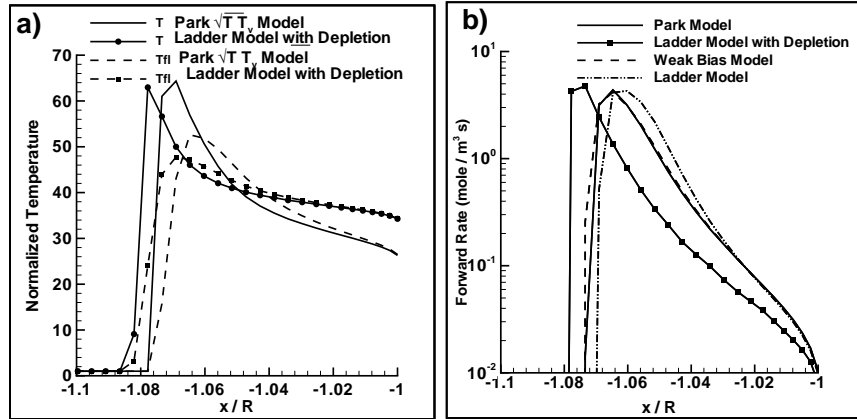


Figure 25: Effect of Vibrational Bias and Depletion in Blunt Body Flow on Temperature and Dissociation Rate)

the other models, though all predict similar values for the peak production rate in the shock layer due to the near equilibrium conditions. It is concluded that the Ladder model (without depletion) and weak bias models give an lower and upper bound on the dissociation rate in the narrow region of shock jump location.

At a lower Mach number of 11.18 for air flow past a blunt body, there is considerable oxygen dissociation with negligible nitrogen dissociation. Temperature profiles along the stagnation streamline, Figure 26, shows the relatively small influence of bias and the large influence of vibrational population depletion in oxygen dissociation, (See Figure 24 for dissociation reduction factor). The shock standoff distance predicted with the effect of depletion in the Ladder model exhibits a better agreement with experiment, Figure 27 than the weak bias, Park, and ladder models.

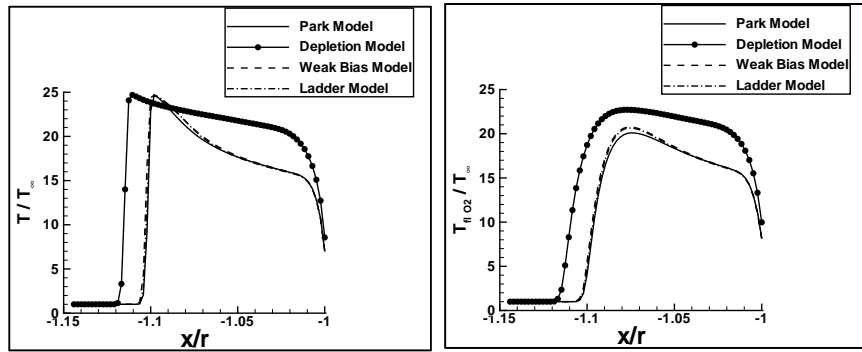


Figure 26: Comparison of Translational and Vibrational Temperature Along the Stagnation Streamline

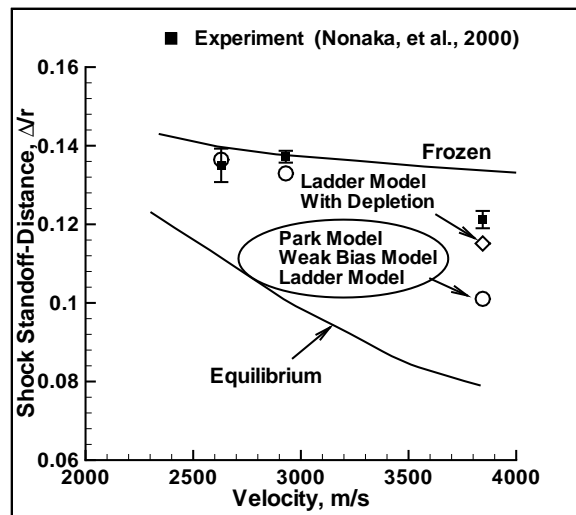


Figure 27: Comparison of Shock-Standoff Distances

4 Conclusions

A high-order finite-difference method has been developed for use in 3-D multidisciplinary applications. The key ingredients in the approach are Padé-type differencing and filtering formulas. The method has been extended to treat the complications associated with nonuniform meshes, nonlinearities and truncated boundaries. In particular, issues related to boundary condition implementation and instability due to mesh stretching have been overcome. Special care is exerted to develop the proper metric evaluation procedures to retain the advantages of higher order accuracy in curvilinear and dynamically deforming 3-D meshes. An effective overlap-based strategy is combined with boundary formulations to facilitate domain-decomposition in parallel processing strategies for arbitrary meshes. A wide range of numerical experiments demonstrate that the method overcomes the traditional problems which had limited the utilization of high-order methods to multidisciplinary phenomena in practical situations.

For high-temperature physics, a first-principles-based method has been developed to solve the interaction between internal modes. Numerical simulations have been completed of steady state, hypersonic flows for the prediction of multitranslational and rotational temperatures, and vibrational energy distributions. Separately, a new gas kinetic, multitranslational temperature model for a monoatomic gas has been developed by solving equations derived from the Boltzmann equation with a first order Chapman-Enskog expansion of an anisotropic velocity distribution function. The model, extended to rotational nonequilibrium, has been employed for highly nonequilibrium shock structures and compared with DSMC solutions and experimental data. The nonequilibrium vibrational energy distributions have been modeled by the master equation and the population distributions in the quantum energy states of the diatomic molecule evaluated under multiquantum vibrational-translational energy exchanges. The dissociation process considered the effect of vibrational bias and depletion on the equilibrium dissociation rate. Results of hypersonic blunt body flow have compared with experimental shock stand-off distance. It has been shown that the Ladder model with population depletion provided the most favorable comparison with experiment compared with the Park model, weak bias model, and Ladder model without depletion. These results guide a better understanding and characterization of the nonequilibrium processes prevalent in hypersonic aerospace vehicle flowfields.

5 References

- [1] Tam, C., “Computational Aeroacoustics: Issues and Methods,” *AIAA J.*, Vol. 33, No. 10, 1995, pp. 1788–1796.
- [2] Hirsh, R., “Higher Order Accurate Difference Solutions of Fluid Mechanics Problems by a Compact Differencing Technique,” *Journal of Computational Physics*, Vol. 19, 1975, pp. 90–109.
- [3] Lele, S., “Compact Finite Difference Schemes with Spectral-like Resolution,” *Journal of Computational Physics*, Vol. 103, 1992, pp. 16–42.
- [4] Alpert, P., “Implicit Filtering in Conjunction with Explicit Filtering,” *J. Comp. Phys.*, Vol. 44, 1981, pp. 212–219.
- [5] Anderson, D., Tannehill, J., and Pletcher, R., *Computational Fluid Mechanics and Heat Transfer*, McGraw-Hill Book Company, 1984.
- [6] Mitchner, M. and Kruger, C., *Partially Ionized Gases*, John Wiley & Sons, 1973.
- [7] Collatz, L., *Numerical Treatment of Differential Equations*, Springer Verlag, 3rd ed., 1966.
- [8] Carpenter, M., Gottlieb, D., and Abarbanel, S., “The Stability of Numerical Boundary Treatments for Compact High-Order Finite-Difference Schemes,” *Journal of Computational Physics*, Vol. 108, 1993, pp. 272–295.
- [9] Gaitonde, D. and Visbal, M., “High-Order Schemes for Navier-Stokes Equations: Algorithm and Implementation into FDL3DI,” Tech. Rep. AFRL-VA-WP-TR-1998-3060, Air Force Research Laboratory, Wright-Patterson AFB, 1998.
- [10] Visbal, M. and Gaitonde, D., “High-Order Accurate Methods for Complex Unsteady Subsonic Flows,” *AIAA Journal*, Vol. 37, No. 10, 1999, pp. 1231–1239.
- [11] Gaitonde, D., Shang, J., and Young, J., “Practical Aspects of High-Order Accurate Finite-Volume Schemes for Electromagnetics,” *AIAA Paper 97-0363*, Jan. 1997.
- [12] Gaitonde, D. and Visbal, M., “Further Development of a Navier-Stokes Solution Procedure Based on Higher-Order Formulas,” *AIAA Paper 99-0557*, January 1999.
- [13] Gaitonde, D. and Visbal, M., “Pade-type Higher-Order Boundary Filters for the Navier-Stokes Equations,” *AIAA J.*, Vol. 38, No. 11, Nov. 2000, pp. 2103–2112.
- [14] Fyfe, D., “Economical Evaluation of Runge-Kutta Formulae,” *Math. Comput.*, Vol. 20, 1966, pp. 392–398.
- [15] Beam, R. and Warming, R., “An Implicit Factored Scheme for the Compressible Navier-Stokes Equations,” *AIAA Journal*, Vol. 16, No. 4, 1978, pp. 393–402.

- [16] Pulliam, T. and Chaussee, D., “A Diagonal Form of an Implicit Approximate-Factorization Algorithm,” *Journal of Computational Physics*, Vol. 39, No. 2, 1981, pp. 347–363.
- [17] Gaitonde, D. and Poggie, J., “An Implicit Technique for 3-D Turbulent MGD with the Generalized Ohm’s Law,” *AIAA Paper 2001-2736*, June 2001.
- [18] Pulliam, T., “Artificial Dissipation Models for the Euler Equations,” *AIAA J.*, Vol. 24, 1986, pp. 1931–1940.
- [19] Visbal, M. and Gordnier, R., “A High-Order Flow Solver for Deforming and Moving Meshes,” *AIAA Paper 2000-2619*, June 2000.
- [20] Pulliam, T. H. and Steger, J. L., “Implicit Finite-Difference Simulation of Three-Dimensional Compressible Flows,” *AIAA Journal*, Vol. 18, No. 2, February 1980, pp. 159–167.
- [21] Visbal, M. and Gaitonde, D., “Very High-Order Spatially Implicit Schemes for Computational Acoustics on Curvilinear Meshes,” *J. Comp. Acoustics*, Vol. 9, No. 4, 2001, pp. 1259–1286.
- [22] Thomas, P. and Lombard, C., “Geometric Conservation Law and its Application to Flow Computations on Moving Grids,” *AIAA Journal*, Vol. 17, No. 10, 1979, pp. 1030–1037.
- [23] Visbal, M. and Gaitonde, D., “High-Order Accurate Methods for Unsteady Vortical Flows on Curvilinear Meshes,” *AIAA Paper 98-0131*, January 1998.
- [24] Roe, P., “Approximate Riemann Solvers, Parameter Vectors and Difference Schemes,” *Journal of Computational Physics*, Vol. 43, 1981, pp. 357–372.
- [25] van Leer, B., “Flux-Vector Splitting For the Euler Equations,” Tech. Rep. 82-30, ICASE, September 1982.
- [26] Gustafsson, B., “The Convergence Rate for Difference Approximations to Mixed Initial Boundary Value Problems,” *Math. Comp.*, Vol. 29, No. 130, 1975, pp. 396–406.
- [27] Kravchenko, A., Moin, P., and Shariff, K., “B-spline Method and Zonal Grids for Simulations of Complex Turbulent Flows,” *AIAA Paper 97-0433*, 1997.
- [28] Visbal, M., “Computed Unsteady Structure of Spiral Vortex Breakdown on Delta Wings,” *AIAA Paper 96-2074*, June 1996.
- [29] Visbal, M., Gaitonde, D., and Gogineni, S., “Direct Numerical Simulation of a Forced Transitional Plane Wall Jet,” *AIAA Paper 98-2643*, June 1998.
- [30] Shang, J. and Gaitonde, D., “Characteristic-Based, Time-Dependent Maxwell Equations Solvers on a General Curvilinear Frame,” *AIAA Journal*, Vol. 33, No. 3, March 1995, pp. 491–498.

- [31] Gaitonde, D., “Development of a Solver for 3-D Non-ideal Magnetogasdynamics,” *AIAA Paper 99-3610*, June 1999.
- [32] Gaitonde, D. and Poggie, J., “Simulation of Magnetogasdynamic Flow Control Techniques,” *AIAA Paper 2000-2326*, 2000.
- [33] Shercliff, J., *A Textbook of Magnetohydrodynamics*, Pergamon Press, 1965.
- [34] Careri, D., “Note on the Rate of Recombination of Free Atoms,” *Journal of Chemical Physics*, Vol. 21, 1953, pp. 749.
- [35] Rice, O., “Reply to Careri’s “Note on the Rate of Recombination of Free Atoms”,” *Journal of Chemical Physics*, Vol. 21, 1953, pp. 750.
- [36] Osipov, A. I. and Stupochenko, E., “Kinetics of the Thermal Dissociation of Diatomic Molecules I. Small Impurity of Diatomic Molecules in a Monoatomic Inert Gas,” *Combustion, Explosion and Shock Waves, Translated from Fizika Goreniya i Vzryva*, Vol. 10, No. 3, 1974, pp. 303–313.
- [37] Osipov, A. I. and Stupochenko, E., “Kinetics of the Thermal Dissociation of Diatomic Molecules II. Single Component System and Mixtures of Polyatomic Gases,” *Combustion, Explosion and Shock Waves, Translated from Fizika Goreniya i Vzryva*, Vol. 10, No. 4, 1974, pp. 399–409.
- [38] Josyula, E. and Bailey, W. F., “Vibration-Dissociation Coupling Using Master Equations in Nonequilibrium Hypersonic Blunt-body Flow,” *Journal of Thermophysics and Heat Transfer*, Vol. 15, No. 2, April 2001, pp. 157–167.
- [39] Josyula, E. and Bailey, W., “Vibrational Population Enhancement in Nonequilibrium Dissociating Hypersonic Nozzle Flows,” *Journal of Thermophysics and Heat Transfer*, to appear in 2004.
- [40] Josyula, E. and Bailey, W., “Vibrational Relaxation and Population Depletion of Nitrogen in Hypersonic Flows,” *AIAA Paper 2002-0200*, January 2002.
- [41] Rich, J., Macheret, S., and Adamovich, I., “Aerothermodynamics of Vibrationally Nonequilibrium Gases,” *Experimental Thermal and Fluid Science*, Vol. 13, 1996, pp. 1–10.
- [42] Ionin, A., Klimachev, Y. M., Konev, Y. B., Kurnosov, A., Napartovich, A., Sinitsyn, D., and Terekhov, Y. V., “Multiquantum Vibrational Exchange in Highly Excited CO Molecules,” *Quantum Electronics*, Vol. 30, No. 7, 2000, pp. 574–579.
- [43] Lechner, A., “Vibrational Relaxation and Small-Signal-Gain of Anharmonic Oscillator Molecules (CO, N₂, HBr, NO) Including MULTi-Quantum Transitions,” *International Symposium of Gasdynamics and Chemical Lasers*, October 1976.
- [44] Zalesskaya, G., “Relaxation Processes at High Levels of Vibrational Excitation of Polyatomic Molecules in the Ground Electronic State,” *Journal of Applied Spectroscopy*, Vol. 69, No. 3, 2002, pp. 328–336.

- [45] Abraham, A. and Fisher, E., “Modeling of a Pulsed CO/N_2 Molecular Laser System,” *Journal of Applied Physics*, Vol. 43, No. 11, November 1972, pp. 4621–4631.
- [46] Candler, G., Olejniczak, J., and Harrold, B., “Detailed Simulation of Nitrogen Dissociation in Stagnation Regions,” *Physics of Fluids*, Vol. 9, No. 7, July 1997, pp. 2108–2117.
- [47] Adamovich, I., Macheret, S., Rich, J., and Treanor, C., “Vibrational Relaxation and Dissociation Behind Shock Waves Part 1: Kinetic Rate Models,” *AIAA Journal*, Vol. 33, No. 6, June 1995, pp. 1064–1069.
- [48] Adamovich, I., Subramaniam, V., Rich, J., and Macheret, S., “Phenomenological Analysis of Shock-Wave Propagation in Weakly Ionized Plasmas,” *AIAA J.*, Vol. 36, No. 5, 1998, pp. 816–822.
- [49] Xu, K., “Regularization of the Chapman-Enskog Expansion and its Application of Shock Structure,” *Physics of Fluids*, Vol. 14, No. 4, 2002, pp. L17–L20.
- [50] Bhatnagar, P., Gross, E., and Krook, M., “A Model for Collision Processes in Gases I: Small Amplitude Processes in Charged and Neutral One-Component Systems,” *Phys. Rev.*, Vol. 94, 1954, pp. 511–525.
- [51] Candler, G., Nijhawan, S., and Bose, D., “A Multiple Translational Temperature Gas Dynamics Model,” *Physics of Fluids*, Vol. 6, No. 11, November 1994, pp. 3776–3786.
- [52] Xu, K., “A Gas-Kinetic BGK Scheme for the Navier-Stokes Equations and its Connection with Artificial Dissipation and Godunov Method,” *Journal of Computational Physics*, Vol. 171, 2001, pp. 289–335.
- [53] Alsmeyer, H., “Density profiles in argon and nitrogen shock waves measured by the absorption of an electron beam,” *J. Fluid Mech.*, Vol. 74, 1976, pp. 497.
- [54] Josyula, E., “Computational Study of Vibrationally Relaxing Gas Past Blunt Body in Hypersonic Flows,” *Journal of Thermophysics and Heat Transfer*, Vol. 14, No. 1, January 2000, pp. 18–26.
- [55] Doroshenko, V., Kudryavtsev, N., Novikov, S., and Smetanin, V., “Effect of the Formation of Vibrationally Excited Nitrogen Molecules in Atomic Recombination in a Boundary Layer on the Heat Transfer,” *High Temperature (USSR)*, Vol. 28, No. 1, 1990, pp. 82–89.
- [56] Huber, K. and Herzberg, G., *Constants of Diatomic Molecules*, Van Nostrand Reinhold Company, New York, 1979.
- [57] Park, C., *Nonequilibrium Hypersonic Aerothermodynamics*, John Wiley and Sons, Inc., New York, 1990.
- [58] Robben, F. and Talbot, L., “Experimental Study of the Rotational Distribution Function of Nitrogen in a Shock Wave,” *Physics of Fluids*, Vol. 9, 1966, pp. 653.

List of Acronyms, Abbreviations and Symbols

a, b, c	coefficients of explicit terms in the compact difference formula
a_n	coefficients of explicit terms in the compact filter formula
c_p	specific heat at constant pressure
e	total energy per unit mass
E	total specific energy
E_x, E_y, E_z	nondimensional components of the electric field vector
f	molecular velocity distribution function
$\mathbf{F}, \mathbf{G}, \mathbf{H}$,	inviscid vector fluxes
$\mathbf{F}_v, \mathbf{G}_v, \mathbf{H}_v$	viscous vector fluxes
g	anisotropic distribution function
i	grid point index number
\mathcal{J}	Jacobian of the coordinate transformation
k	Boltzmann constant
k_{d_v}	dissociation rate from state v [cm^3/s]
K	Equilibrium constant
Kn	Knudsen number
m_i	Molecular weight of species i
M	Mach number
\mathcal{M}	molecular weight, $kg/mole$
N	number density
NCO	Noncommunicating overlap
p	pressure, N/m^2
Pr	Prandtl number, 0.73 for air
$\bar{\mathbf{q}}$	heat flux vector, W
\mathbf{Q}	vector of dependent variables
Q_i	components of the heat flux vector
R	gas constant
Re	reference Reynolds number, $\rho_\infty u_\infty l / \mu_\infty$
\mathbf{S}	source vector
T	equilibrium trans-rotational temperature
t	nondimensional time
T_t	translational temperature
T_v	vibrational temperature
u, v, w	nondimensional Cartesian velocity components
v, v', w, w'	vibrational quantum numbers
V-T	Vibrational-Translational
V-V	Vibrational-Vibrational
x, y, z	nondimensional Cartesian coordinates
Z_{vib}	vibrational partition function
α, β	coefficients in difference formula

α_f, β_f	coefficients in filter formula
ϵ_v	quantum level energy
γ	ratio of specific heats
κ	thermal conductivity coefficient
λ_1	upstream mean free path, m
μ	viscosity, kg/m-s
ϕ	general scalar variable
τ	characteristic time scale
τ_{ij}	Navier-Stokes stress tensor, N/m^2
Θ_d	characteristic temperature of dissociation
Θ_v	characteristic temperature of vibration
φ_v	depletion factor
ρ	total density, total molecular population
ξ, η, ζ	nondimensional body-fitted computational coordinates
$\xi_t, \xi_x, \xi_y, \xi_z$	metric coefficients of the coordinate transformation

Subscripts

max	maximum value
min	minimum value